Recovery of a learned behavior despite partial restoration of neuronal dynamics after chronic inactivation of inhibitory neurons

Zsofia Torok[1]*, *Laura Luebbert*[1], *Jordan Feldman*[1], *Alison Duffy*[3], *Alexander A. Nevue*[4], *Shelyn Wongso*[1], *Claudio V. Mello*[4]‡, *Adrienne Fairhall*[3]‡, *Lior Pachter*[1,2]‡, *Walter G. Gonzalez*[5]‡, *Carlos Lois*[1]*‡

[1]Division of Biology and Biological Engineering, California Institute of Technology; Pasadena, CA, USA.
[2]Department of Computing and Mathematical Sciences, California Institute of Technology; Pasadena, CA, USA.
[3]University of Washington; Seattle, WA, USA.
[4]Oregon Health & Science University; Portland, OR, USA.
[5]Department of Physiology, University of San Francisco; San Francisco, CA, USA.
‡Senior authors
*Corresponding authors. Email: clois@caltech.edu (C.L.); szofitorok8@gmail.com, zsofi@caltech.edu (Z.T.)

Abstract

Maintaining motor skills is crucial for an animal's survival, enabling it to endure diverse perturbations throughout its lifespan, such as trauma, disease, and aging. What mechanisms orchestrate brain circuit reorganization and recovery to preserve the stability of behavior despite the continued presence of a disturbance? To investigate this question, we chronically silenced a fraction of inhibitory neurons in a pre-motor circuit necessary for singing in zebra finches. This manipulation altered brain activity and severely perturbed their song, a complex learned behavior, for around two months, after which it was precisely restored. Electrophysiology recordings revealed abnormal offline dynamics resulting from chronic inhibition loss, while subsequent recovery of the behavior occurred despite partial normalization of brain activity. Single-cell RNA sequencing revealed that chronic silencing of interneurons leads to elevated levels of microglia and MHC I. These experiments demonstrate that the adult brain can overcome extended periods of drastic abnormal activity. The reactivation of mechanisms employed during learning, including offline neuronal dynamics and upregulation of MHC I and microglia, could facilitate the recovery process following perturbation of the adult brain. These findings indicate that some forms of brain plasticity may persist in a dormant state in the adult brain until they are recruited for circuit restoration.

Introduction

Maintaining the ability to precisely execute motor behavior throughout life, despite perturbations due to trauma, disease, or aging, is crucial for reproduction and survival. To reliably execute behaviors, brain circuits require a balance of excitation and inhibition (E/I balance) to maintain physiological activity patterns. Loss of E/I balance causes abnormal patterns of neuronal activity, which can result in diseases such as epilepsy [1,2]. Given its importance, brain circuits strive to restore E/I balance once disturbed [3]. However, the mechanisms orchestrating circuit reorganization and recovery of E/I balance during the continued presence of a perturbation remain poorly understood.

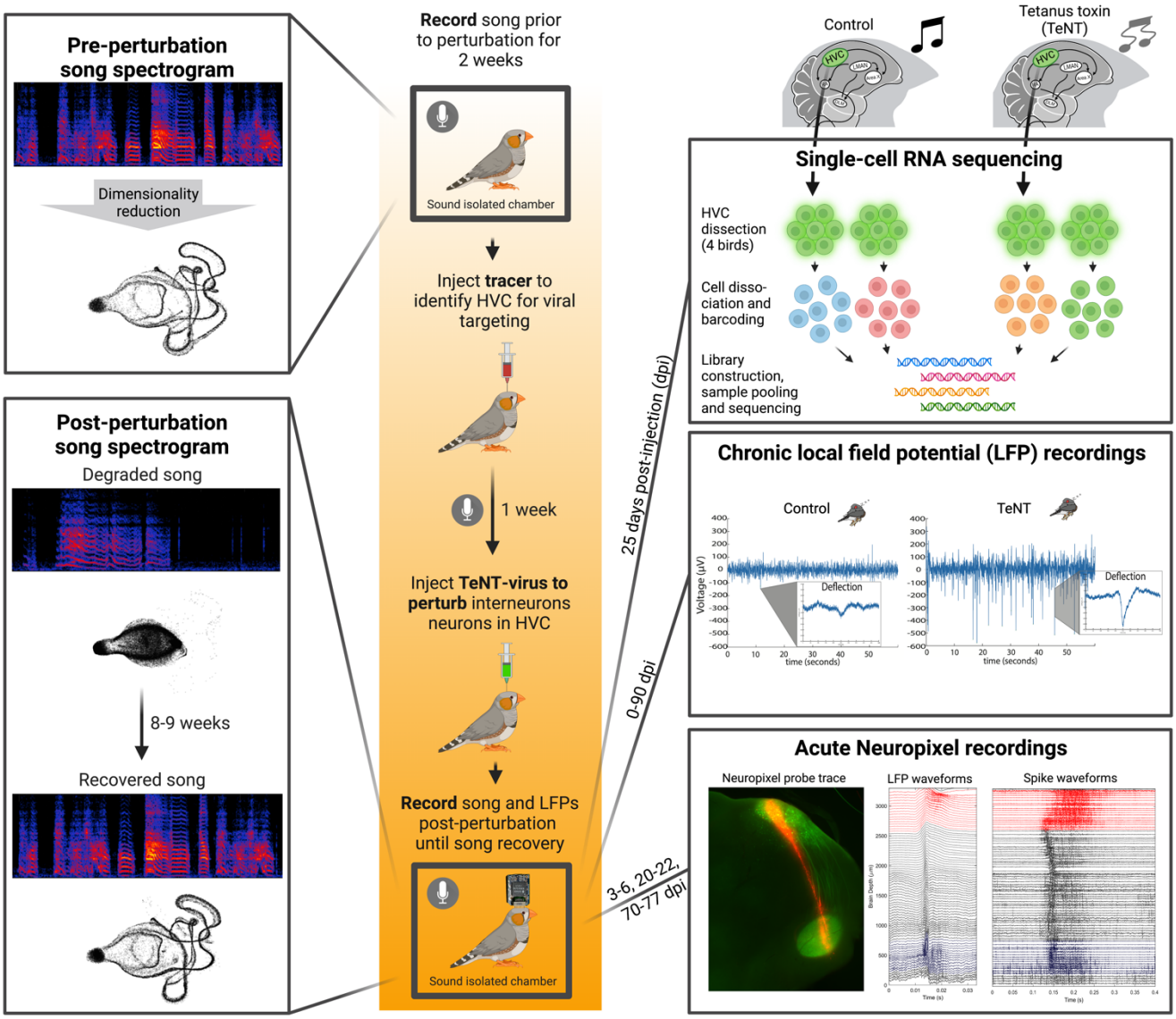

Graphical Abstract: *Schematic overview of the experiments performed in this study. To investigate how a complex motor behavior recovers after chronic loss of inhibitory tone, we blocked the function of zebra finch HVC inhibitory neurons by bilateral stereotaxic injection of an AAV viral vector into HVC. Throughout various timepoints in this perturbation paradigm, we recorded song behavioral data, electrophysiological measurements (chronic and acute within HVC), and measured changes in gene expression at single-cell resolution.*

Zebra finches produce a highly stereotyped song with minimal variability over extended periods of time [4], underpinned by temporally precise neural activity [5]. This species thus provides an optimal model to simultaneously track abnormal brain activity, its effect on behavior, and changes to both over time. It serves as an excellent model for studying chronic E/I imbalance and accompanying changes over time at the behavioral, neuronal, and transcriptomic levels.

Here, we genetically block inhibitory neurons in HVC (proper name), a premotor brain nucleus of the male zebra finch involved in song production, to chronically perturb the E/I balance. HVC contains two

main types of excitatory neurons that project to two main downstream targets: nucleus X (proper name) and nucleus RA (robust nucleus of the arcopallium). In addition, HVC includes several types of inhibitory neurons whose axons do not leave HVC; thus, they act locally within HVC [5]. Juvenile male zebra finches learn their song from their fathers during the "critical period" and once learned, produce a highly stereotypical song for the rest of their lives [6]. Previous work has shown that inhibition plays a role during development to close the critical period and protect learned components of the song in juvenile animals [7]. Acutely blocking interneuron signaling in adult animals by chemicals leads to abnormal behaviors that quickly return to normal once the chemical is washed out [8]. However, it is not known how long-term disruption of inhibitory neurons affects neuronal dynamics, and whether behaviors can recover after such drastic perturbation.

Results

To investigate how a complex motor behavior recovers after chronic loss of inhibitory tone, we blocked the function of HVC inhibitory neurons in adult male zebra finches by bilateral stereotaxic injection of an AAV viral vector into HVC. The AAV viral vector carried the light chain of tetanus toxin (TeNT), driven by the human dlx5 promoter, which is selectively active in inhibitory neurons [9]. TeNT blocks the release of neurotransmitters from presynaptic terminals, thereby preventing neurons from communicating with their postsynaptic partners [10]. Thus, expression of TeNT does not directly alter the ability of neurons to fire action potentials, but effectively mutes them. As a control, a second group of animals was injected with an AAV carrying the green fluorescent protein NeonGreen driven by the ubiquitous promoter CAG. Throughout various time points in this perturbation paradigm, we recorded song behavioral data, obtained electrophysiological measurements (chronic and acute within HVC), and measured changes in gene expression at single-cell resolution (Graphical Abstract).

Chronic genetic muting of inhibitory neurons in HVC leads to zebra finch song degradation and subsequent unsupervised recovery

An average male zebra finch song typically contains 4 to 7 units called syllables. These syllables are fixed in order and make up a motif, which is repeated multiple times to form a bout [11–13]. A bout defines the length of a vocally active period in adult animals. Throughout all experiments, the song of the individually housed animals was continuously monitored from 7-20 days pre-injection to 60-100 days post-injection (dpi) using sound-isolated chambers. In control animals, the song did not change at any time after the viral injection. For the first 24-48 hours after injection, the song of TeNT-treated animals was virtually identical to their original song. However, starting at 2-5 dpi, the song of TeNT-treated animals began to degrade, both in its acoustic and temporal features (Figure 1). By 10 dpi, the song of TeNT-treated animals was highly degraded and bore no resemblance to the original song before viral injection (Figure 1 A).

During the first few days of song degradation, TeNT-treated animals produced instances of syllables with abnormally long durations far outside the range of any adult syllable duration observed in control animals (Figure 1 A shows one such vocalization at 5 dpi; examples of syllable length distribution:

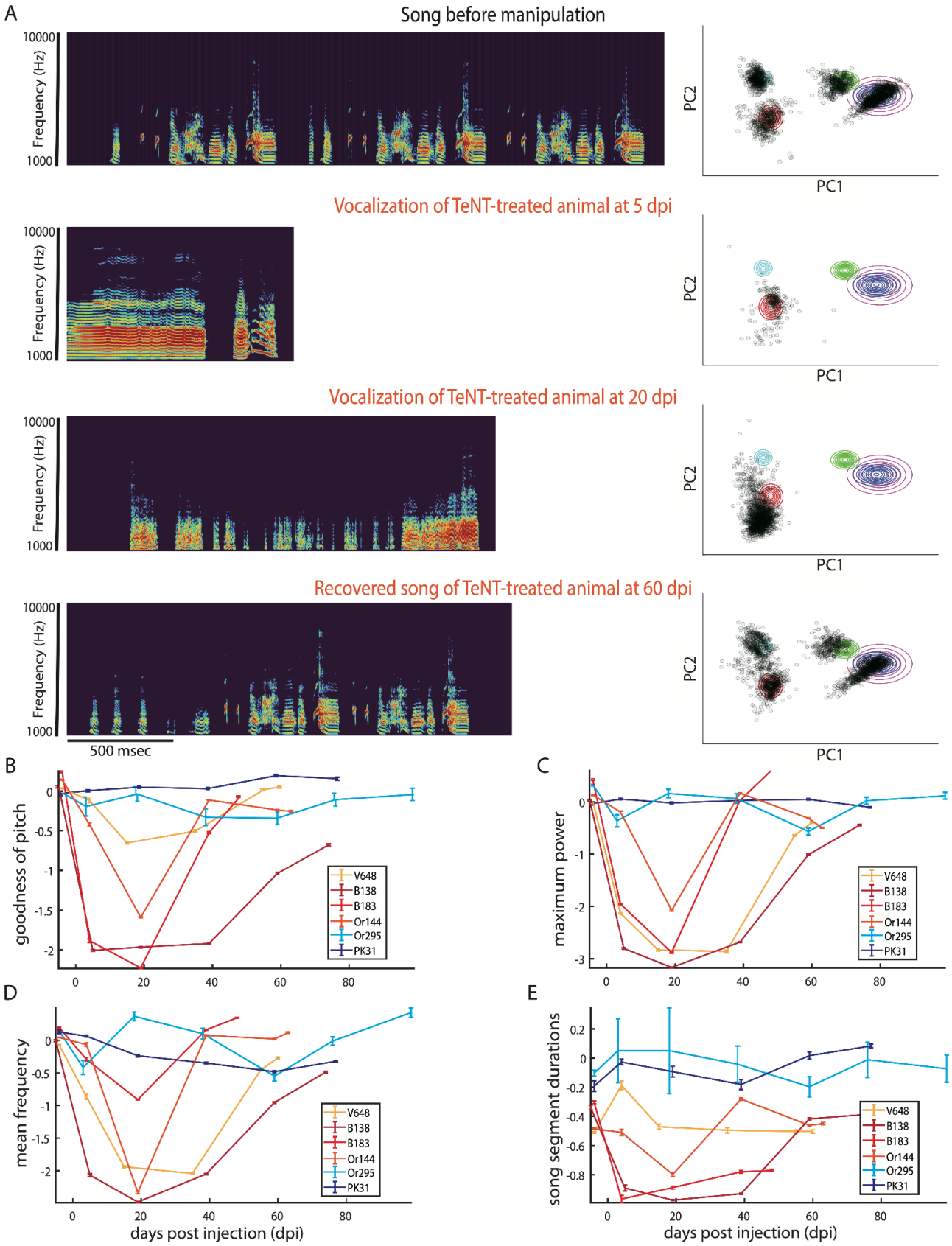

Figure legend on next page.

Figure 1: *Song degradation and recovery after chronic inactivation of inhibitory neurons in HVC by viral expression of tetanus toxin (TeNT).* ***A (left)*** *Examples of spectrograms of songs produced by an animal treated with TeNT before, and 5, 20 and 60 days post- injection (dpi). Data from this animal (V648) are also shown in B-E.* ***A (right)*** *2D principal component analysis (PCA) visualization of syllables produced by the animal on the same day as the spectrogram example on the left. Note: even when the songs are degraded, we continue to refer to an uninterrupted length of vocalization as a 'syllable'. Individual dots indicate single syllable renditions. In the unperturbed song (before virus injection), syllables cluster into distinct groups. See Methods for description of acoustic features used in the PCA space.* ***B-E*** *Different features of the vocalizations before and after stereotaxic injection of control (GFP-expressing) or TeNT virus. The mean frequency and goodness of pitch measures represent averages over song segments. Control animals (Or295 and PK31) are labeled in shades of blue (n=2); TeNT-treated animals (V648, B183, B138 and Or144) are labeled in shades of red and orange (n=4). Traces indicate averages over syllables sung within the 3 closest days of recorded vocalizations. Error bars indicate standard error. Values are normalized relative to distributions 5 days before perturbation (see Methods).*

Supplementary Figure 1). Later on (8 to 30 dpi), all vocalizations became very short (< 100 msec) with inter-syllable intervals of varying lengths (100 msec to 1 sec) between them (spectrogram examples in Supplementary Figure 2). At 20-30 dpi, the song of TeNT-treated animals was highly variable between renditions and lacked the normal organization of motif and bout (Figure 1 A). However, by 40-50 dpi, the structure of the song started to re-emerge. By around 70 dpi, the song of TeNT-treated animals was highly similar to the song produced before viral injection (Figure 1).

Nucleus LMAN is required for learning and adult song plasticity [14–16]. To investigate the role of LMAN in song recovery, we chemically lesioned it before the viral perturbation. We found that the LMAN lesion did not affect the song degradation and recovery trajectory after chronically muting HVC inhibitory neurons with TeNT (Supplementary Figure 3-6). These results indicate that behavioral recovery after perturbation of HVC does not require LMAN, a nucleus necessary for song learning.

Chronic electrophysiological recordings reveal that the degree of song distortion is correlated with the presence of large-amplitude voltage deflections in HVC during nighttime

To investigate electrophysiological changes in HVC that accompany song degradation due to chronic loss of inhibition and subsequent behavioral recovery, we continuously recorded electrical activity in HVC across the entire duration of song degradation and recovery (0-90 dpi).

We implanted a 4-shank electrode array containing 16 recording sites in both control and TeNT-injected animals. We simultaneously collected electrophysiological, head movement (recorded with the accelerometer built into the head stage), and audio recordings over a period of 90 dpi. We analyzed the spectral decomposition of the local field potentials (LFPs) during song production from an average of five vocalization epochs [17,18]. LFP recordings provide a readout of transient electrical signals generated by the summed and synchronous local and distant synaptic and action potential activity. In control animals, as expected, both the song behavior and LFP characteristics remained stable: the electrical activity during singing showed voltage deflections which were present throughout the song

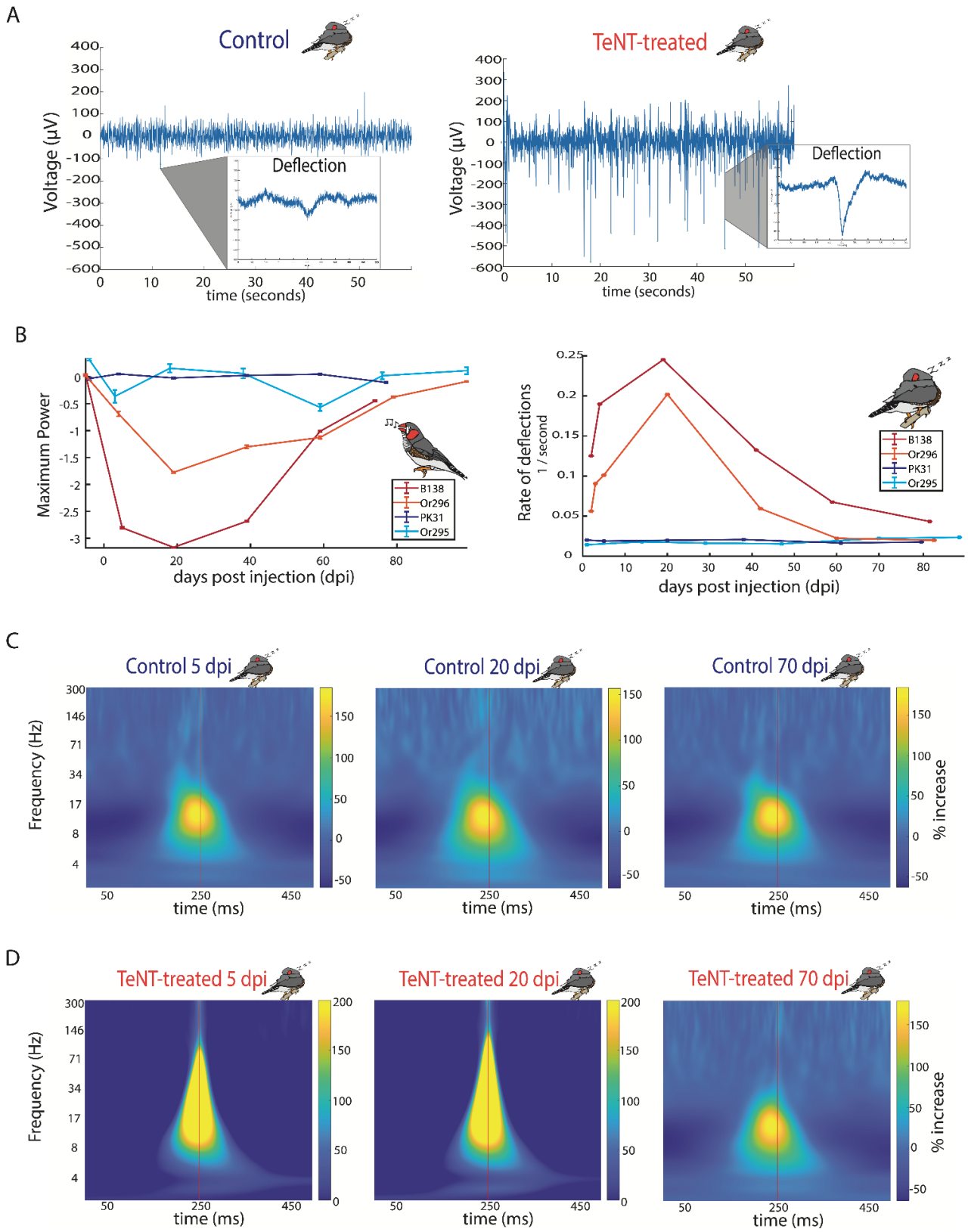

Figure legend on next page.

Figure 2: *Chronic electrophysiology recordings within HVC after chronic inactivation of inhibitory neurons by viral expression of TeNT.* ***A*** *Raw electrophysiology traces during night time (lights off period) from TeNT-treated and control animals 5 days post-injection (dpi). Note: electrodes were implanted on the same day of viral injection. Insets show examples of stereotypical deflections that at 5 dpi were approx. 50 ms in duration, and -530 µV in amplitude, in TeNT-treated animals, compared to 96 ms and -140 µV in control animals.* ***B (left)*** *Quantification of song quality of chronically implanted animals over time. Control animals (PK31 and Or195) are depicted in shades of blue. TeNT-treated animals (B138 and Or296) are depicted in shades of orange and red.* ***B (right)*** *Rate of deflection events during night time. Control animals (PK31 and Or195) are depicted in shades of blue. TeNT-treated animals (B138 and Or296) are depicted in shades of orange and red. The highest rate of sleep voltage deflections in TeNT-treated animals occurred during the periods when the songs were most degraded, as shown on the left.* ***C-D*** *Spectral decomposition of local field potentials (LFPs) of the averaged deflections during night time at 5, 20, and 60 dpi in one control (C) and one TeNT-treated animal (D). The vertical red line depicts the trough of the raw deflection trace. Deflections of TeNT-treated animals in the 15-30 Hz range were approx. 27 times larger than those in control animals at 5 dpi. These differences are statistically significant between control and TeNT-treated groups, but not within the control group ($p=0.7631$ between controls, $p<10^{-35}$ between all other pairs). The deflections across all animals and frequencies become more similar by 60 dpi (15-30 Hz: $p=0.1371$ between controls, $p<10^{-6}$ between all other pairs; 30-70 Hz: $p=0.7493$ between controls, $p<10^{-2}$ between all other pairs). For details on statistics see Methods.*

(Supplementary Figure 7 B). In contrast, at 5 dpi, TeNT-treated animals produced long vocalizations that were preceded by large voltage deflections, neither of which were observed in control animals (Supplementary Figure 7 A). Between 10 to 70 dpi, the songs of TeNT-treated animals were highly variable between renditions and between days.

As a result of this instability in behavior, vocalization number and type could not be reliably characterized and aligned across trials. Hence, we focused on electrophysiological events occurring during nighttime (lights-off periods when the animals are not moving or singing), because they showed higher data consistency (Figure 2 A). The neuronal activity recorded during the nighttime period will be referred to as offline or lights-off throughout the manuscript.

Previous studies have hypothesized that HVC offline activity may reinforce the maintenance of adult song and could drive song learning [19–23]. Therefore, analyzing electrophysiological activity in HVC during offline periods throughout the perturbation could reveal disruptions related to degraded behavior.

The recordings in TeNT-treated animals during lights-off offline periods contained voltage deflections that were more frequent and of larger amplitude than those of controls (Figure 2 A and B), similar to those observed during singing. In addition, in TeNT-treated animals, these large amplitude deflections at night occurred more frequently during the period of time when the song was most degraded (Figure 2 B). At 5 dpi, these stereotypical voltage deflections had an average amplitude of around -530 µV and -140 µV in TeNT-treated and control animals, respectively - a 280% increase in TeNT-treated animals (Supplementary Figure 8). In TeNT-treated animals, the rate of lights-off offline voltage deflections returned to those seen in control as the song regained stereotypy around 50 dpi (Figure 2 B).

To further characterize these voltage deflections, we analyzed the LFPs (1-200 Hz) during the voltage deflection events occurring during lights-off periods, and we performed spectral decomposition of the LFPs. At 5 dpi, we observed an increase in power in the low gamma band (30-70 Hz) in TeNT-treated animals, which returned to control levels as the songs regained stereotypy (Figure 2 C and D).

The highest level of song distortion coincided with the highest rate of large-amplitude voltage deflections during lights-off (Figure 2 B). These findings suggest a relationship between the behavioral timeline of recovery, and the return to control-like offline electrophysiological activity. These results suggest that the restoration of excitation/inhibition (E/I) balance and circuit function is mediated by unsupervised mechanisms, consistent with our earlier publication [24].

Spontaneous local neuronal activity in HVC and RA during lights-off periods show opposite trends upon chronic interneuron perturbation in HVC

To record local neuronal activity at single-neuron resolution over the course of song degradation and recovery, we used high-density silicon probes (Neuropixels) [25,26] to simultaneously record neurons in HVC, RA, and intervening brain areas (Figure 3 A). As described above, the most reliable measurements of abnormal brain activity in TeNT-treated animals were obtained during lights-off periods. Therefore, we performed Neuropixel recordings in head-fixed animals when the lights were off during their natural sleep cycle. To achieve the best possible signal-to-noise ratio, which would allow single-neuron resolution, we focused on acute recordings that were obtained within a few hours after probe insertion. We performed acute recordings at 3-6, 20-22, and 70-77 dpi in TeNT-treated animals, and at 10 and 30 dpi in control animals. We also included recordings from one naïve animal (not injected with any virus) to control for potential artifacts caused by the surgery or viral injection.

We measured the overall neuronal firing rate in HVC and RA of control and TeNT-treated animals. In TeNT-treated animals, HVC started out in a heightened state of spontaneous lights-off activity (likely due to the loss of inhibition), but over the time course of the perturbation activity gradually decreased to levels below control (Figure 3 B). While activity in HVC was elevated between 3-5 dpi and eventually decreased between 20-70 dpi, RA showed the opposite trend, possibly to compensate for the observed changes in HVC activity (Figure 3 B). This suggests the existence of mechanisms that coordinate the spontaneous activity levels between connected brain areas to achieve a balanced output required for the appropriate control of behavior.

In addition, we observed a total of seven events that resemble seizure-like activity in HVC (n=3 TeNT-treated animals at 3-20 dpi) which propagated downstream into RA (Figure 3 C). These periods of elevated neuronal firing in TeNT-treated animals in the early days after perturbation suggest that the

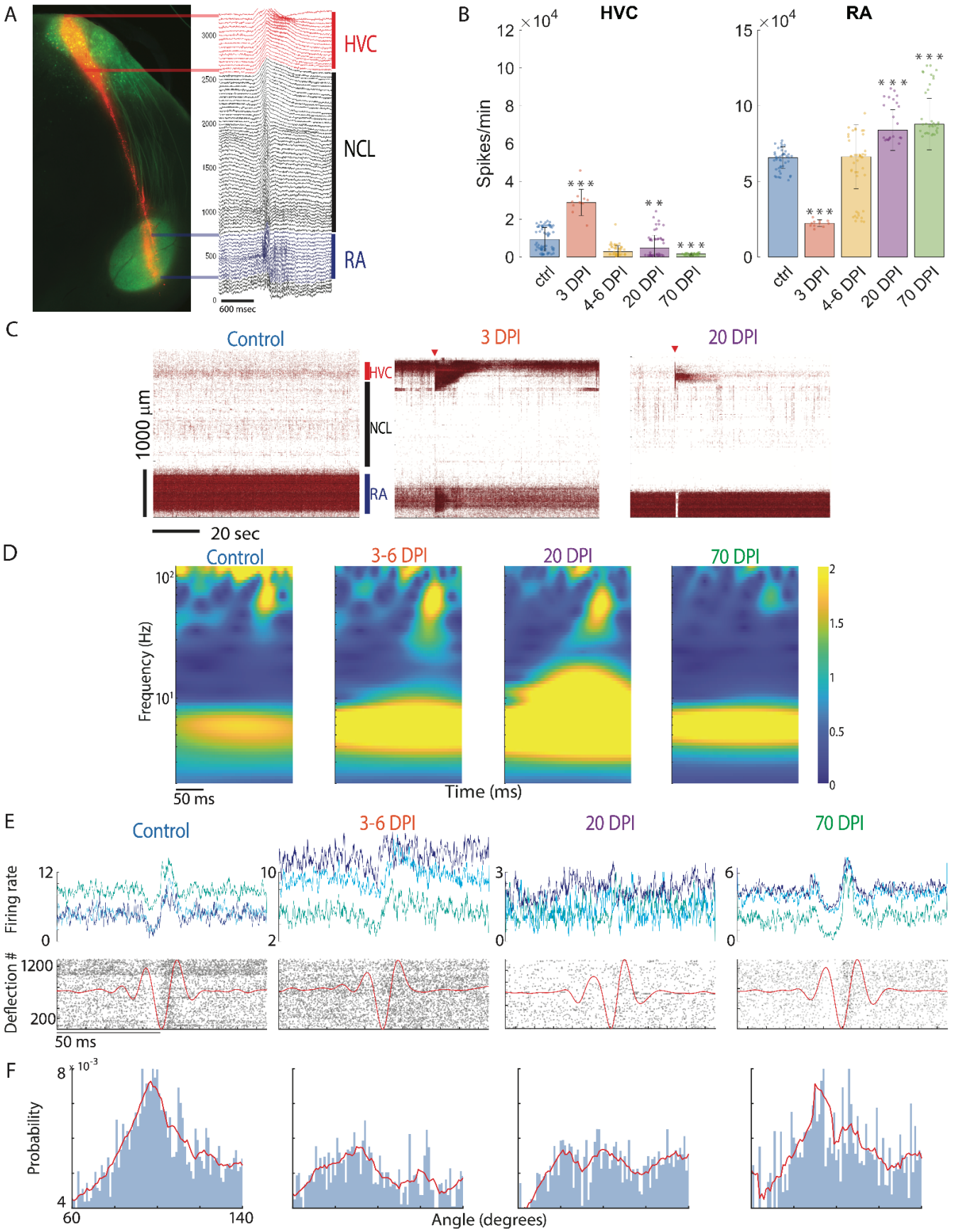

Figure legend on next page.

Figure 3: *Acute electrophysiology recordings after chronic inactivation of inhibitory neurons in HVC by viral expression of TeNT.* ***A*** *A histological section example of a brain slice from a control animal shows the track of the probe (NPIX coated with DiI) insertion (red) and GFP from the viral injection (green). Note: There is green signal in RA because the control animal received injection of a virus in which GFP is driven by the ubiquitous promoter CAG in HVC. This virus infects all cell types in HVC, and axons from HVCRA neurons innervate RA. The raw electrophysiology traces are color-coded by brain area (HVC in red, NCM in black, RA in blue).* ***B*** *Average firing rates of neurons within HVC and RA in control animals (n=3) and TeNT-treated animals at 3 (n=1), 4-6 (n=4), 20 (n=4) and 70 (n=4) dpi. In HVC, the increase in average firing rate at 3 dpi after TeNT injection significantly differs from control (p-value from rank sum test: $0.4*10^{-6}$), as well as the decrease in average firing rate after TeNT injection at 20 dpi (p = 0.002) and 70 dpi ($p = 0.57*10^{-11}$). In RA, the decrease in average firing rate at 3 dpi significantly differs from control ($p = 0.43*10^{-6}$), as well as the increase in average firing rate at 20 dpi ($p = 0.09*10^{-9}$) and 70 dpi ($p = 1.45*10^{-13}$). The stars above the bar plots indicate statistical significance (* = p < 0.005, ** = p< 0.01, *** = p < 0.001).* ***C*** *Examples of neuronal activity in a control animal, TeNT-treated animals at 3 and 20 dpi. The red arrows highlight the "superbursts" or extreme firing levels within HVC and RA which we observed in 3 animals (two animals at 3-4 dpi and one at 20 dpi) in a total of seven instances.* ***D*** *Spectral decomposition of LFPs of the average normalized deflections during lights-off acute recordings in control animals and TeNT-treated animals at 3-6, 20, and 70 dpi.* ***E (top)*** *Example traces of the firing rate of three individual neurons during deflection events that lock or do not lock to a specific phase of the alpha oscillation (shown in red in bottom plots) in HVC of control animals and TeNT-treated animals at 3-6, 20, and 70 dpi.* ***E (bottom)*** *Examples of neuronal firing (indicated by black dots) for one neuron per condition in HVC.* ***F*** *Normalized firing probability distribution of neurons in HVC during a specific phase (angle) of the alpha (1-10 Hz) oscillations extracted from the LFP signal of the averaged deflection events in control animals and TeNT-treated animals at 3-6 dpi (n=4), 20 dpi (n=4), and 70 dpi (n=2 animals). Neuronal firing precision at specific angles (60-140) of the alpha oscillations are lost or broadened in TeNT-treated animals between 3-20 dpi and re-emerges at 70 dpi, upon song recovery.*

removal of inhibitory tone acutely leads to bursts of hyperactivity that resemble discharges previously reported during seizures[1,2,27].

Firing precision of neurons in HVC specific to alpha frequency oscillations recovers as song stereotypy is regained

We used acute Neuropixel recordings to analyze the neuronal firing specifically during the offline voltage deflection events, similar to those that we initially observed using chronic recordings (Figure 2). Examples of averaged voltage traces of offline deflections recording in the acute dataset are shown in Supplementary Figure 9. Compared to the spectral composition of the LFP signature of voltage deflections observed in the chronic recordings (Figure 2 C and D), in acute Neuropixel recordings, we detected similar changes in amplitude, power, and phase measured by the wavelet coefficient (Figure 3 D). In the LFP decomposition of deflection events detected in these acute recordings, we observed large differences between TeNT-treated and control animals in the alpha (1-10 Hz) and the low gamma (30-40 Hz) frequency ranges (Figure 3 D). We calculated the difference in power from the calculated periodogram between the averaged (per animal) deflection and non-deflection events in the alpha (1-10 Hz) and low gamma (30-40 Hz) range. In the low gamma range (30-40 Hz), after an initial increase, the power returned to control levels at 70 dpi (Supplementary Figure 10 A). The relationship between the alpha and low gamma oscillations during voltage deflections varied in angle, then returned to resemble

controls by 70 dpi (Supplementary Figure 10 B-D). In contrast, in the alpha range, the power stayed significantly higher in TeNT-treated animals, even after the song recovered at 70 dpi (Supplementary Figure 10 A).

We compared the timing of single neuron firing with the phase of the alpha and low gamma oscillations during offline voltage deflection events. To this end, we turned to methods previously described to characterize sharp wave ripple events during offline activity in the hippocampus [28]. Previous studies suggest that precise neuronal firing offline during a specific phase of sharp wave ripples underlies correct memory consolidation and recall in the hippocampus [28–31]. We found that in control animals, the neuronal firing within HVC locked tightly to specific phases of the alpha and low gamma oscillatory events during offline voltage deflections. In TeNT-treated animals, during the song degradation period, the firing precision to low gamma oscillations in HVC or to alpha and low gamma oscillations in RA during deflection events did not change compared to control (Supplementary Figure 9). However, during the song degradation period, the precision of local neuronal firing to alpha oscillations between 60 to 140 degrees was lost or broadened compared to control and song-recovered animals (Figure 3 E and F). As song stereotypy was regained, the firing precision to specific phases of the alpha oscillations during deflections re-emerged (Figure 3 E and F). These findings suggest the importance of local neuronal firing precision to alpha oscillations within HVC for correct circuit function. The observed alpha frequency LFP signals could represent inputs into HVC from other brain areas. The capacity of neurons to exhibit phase-locked firing at a specific alpha frequency oscillation may be required for integrating inputs from diverse brain regions and enables the execution of precise motor behaviors.

Single-cell RNA sequencing suggests mechanisms of neuronal plasticity driven by microglia and MHC class I genes during song perturbation

To investigate cellular mechanisms that might underlie the observed changes in neuronal activity and behavior at the transcriptomic level, we performed single-cell RNA sequencing (scRNAseq) of HVC from control (n=2) and TeNT-treated (n=2) adult male zebra finches at 25 dpi, around the time of peak song distortion. HVC from both hemispheres of all four birds were dissected based on retrograde tracer fluorescence and dissociated to prepare single-cell suspensions, which were indexed and pooled. This allowed the construction of a combined dataset, containing results from all organisms and conditions, without the need for batch correction (Supplementary Figure 12, Supplementary Table 2). Following quality control, we retained a total of 35,804 single-cell profiles spanning four individuals, consisting of two control and two TeNT-treated animals.

While cell type abundance was highly concordant between replicates of the same condition (Supplementary Figure 12, Figure 4 A), we found that animals treated with TeNT displayed a three-fold increase in the number of microglia (Figure 4 B). This increase in microglia was likely not due to an inflammatory reaction caused by the surgical procedure or the AAV injection because control animals also received a viral injection with a highly similar construct. Thus, we hypothesize that the increase in microglia in TeNT-treated animals is a consequence of the chronic muting of inhibitory neurons.

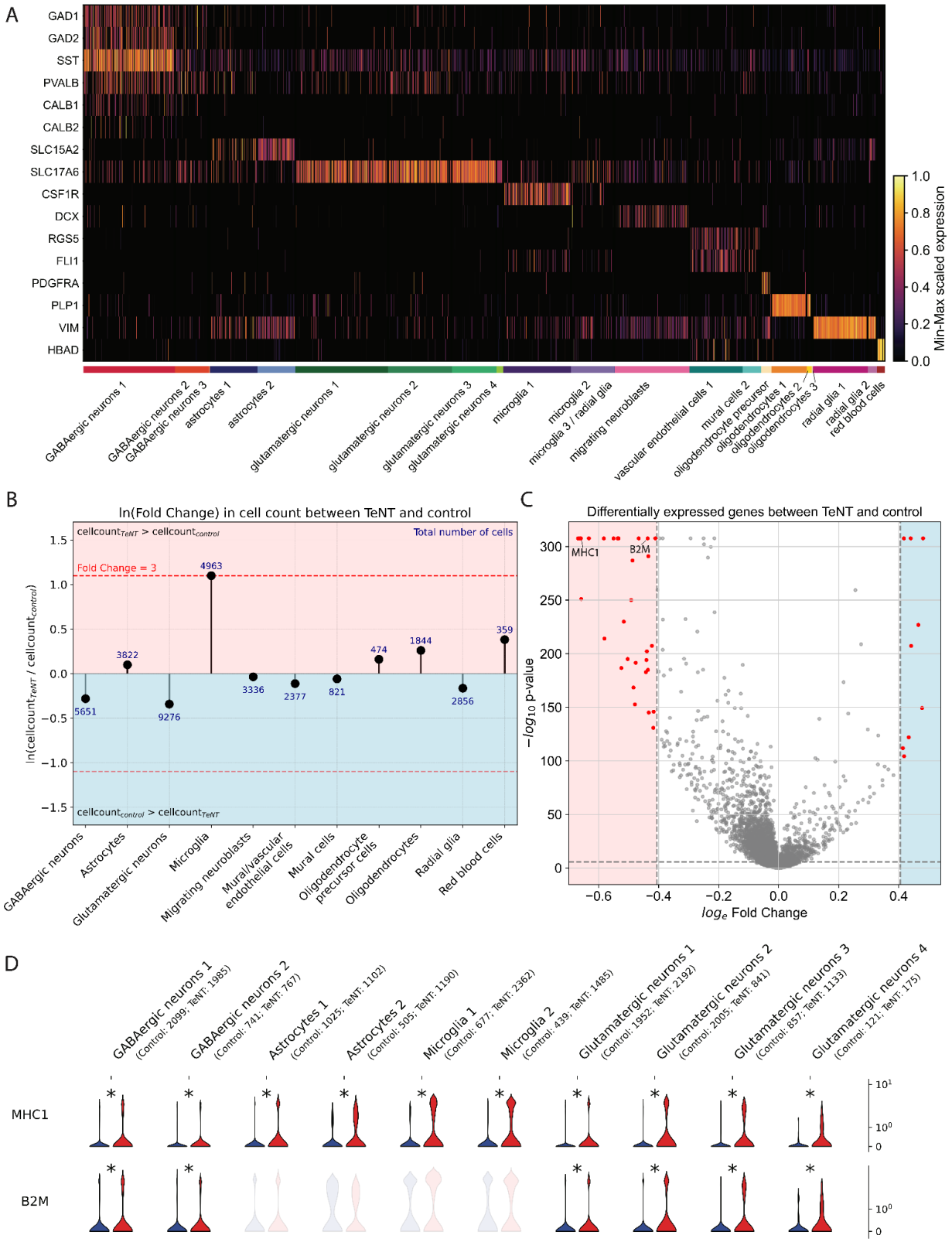

Figure legend on next page.

Figure 4: *Transcriptomic changes at single-cell resolution in HVC at 25 days after chronic inactivation of inhibitory neurons through viral expression of TeNT. Single-cell RNA sequencing of the HVCs of control (n=2) and TeNT-treated (n=2) animals was performed at 25 dpi.* ***A*** *Heatmap showing min-max scaled expression of cell type marker genes for each cell type (data from both control and TeNT-treated animals).* ***B*** *Log-fold change in total number of cells per cell type between TeNT-treated and control animals.* ***C*** *Volcano plot showing statistical significance over magnitude of change of differentially expressed genes between TeNT-treated and control animals across all cell types. Dotted lines indicate fold change = 1.5 and p value = Bonferroni corrected alpha of 0.05. A list of all differentially expressed genes can be found here: https://github.com/lauraluebbert/TL_2023.* ***D*** *Violin plots of normalized counts of major histocompatibility complex 1 α chain-like (MHC1) (ENSTGUG00000017273.2) and beta 2 microglobulin-like (B2M) (ENSTGUG00000004607.2) genes in control (n=2, blue) and TeNT-treated (n=2, red) animals per cell cluster. A star indicates a significant increase in gene expression in TeNT-treated animals compared to control ($p < 0.05$ and fold change > 1.5).*

Several studies have shown that microglia play a role in synaptic plasticity during early brain development and learning in mammals [32–35]. These prior observations in combination with our findings suggest that microglia might participate in the synaptic reorganization triggered by circuit perturbation. We performed *in situ* hybridization (ISH) using a probe against RGS10, a gene expressed in microglia, during song degradation at 25 dpi and after recovery at 90 dpi. At 25 dpi, the number of microglia increased in TeNT-treated animals compared to control (Supplementary Figure 13 A, 14 A and B), and returned to control levels by 90 dpi, when the song had recovered.

To further investigate the hypothesis that microglia are associated with circuit reorganization involved in neuronal plasticity, we counted the number of microglial cells in HVC at different times during song learning in naive (untreated), juvenile birds using ISH. The number of microglia in the HVC of juveniles was higher during the early stages of the song learning period (30-50 days post-hatching (dph)), compared to 70 dph, after the song became more stereotypic (Supplementary Figure 13 B, 14 C and D).

Furthermore, scRNAseq analysis revealed a significant increase in the expression of the α chain of major histocompatibility complex class I (MHC I) and β_2-microglobulin (B2M) across several neuronal cell types in TeNT-treated animals (Figure 4 C and D) and confirmed the increases in MHC I by ISH (Supplementary Figure 13 C, 14 E and F). MHC class I molecules are heterodimers that consist of two polypeptide chains, α and B2M, and are involved in antigen presentation for T cells [36]. This increase in MHC I and B2M is likely triggered by the genetic silencing of inhibitory neurons, and not due to an inflammatory response because it was not observed in control animals injected with a control virus. MHC I and B2M have been observed in previous studies to be highly expressed in neurons during brain development [37,38], consistent with a hypothetical role in synaptic plasticity [39,40]. Here we observe that MHC I and B2M are upregulated in response to perturbation of neuronal activity in a fully formed circuit, indicating their possible role in the restoration of brain function.

Discussion

The brain requires a balance between excitation and inhibition to maintain physiological activity patterns and enable reliable behaviors. We found that chronic muting of inhibitory neurons in a pre-motor circuit severely disrupts a learned motor behavior for an extended period of time (30-90 days). Even after several weeks of perturbed brain activity, the brain circuit is able to regain function and recover the behavior, despite failing to restore some aspects of its neuronal dynamics. We propose that the return to control-like offline voltage deflections and the precision of local neuronal activity during alpha oscillations during these deflections are key components that accompany the behavioral recovery. Our observations indicate a putative relationship between activity dynamics offline and the restoration of circuit function. Furthermore, our data suggest that microglia and MHC I may be involved in changes caused by chronic perturbation of neuronal activity. These experiments reveal that the adult brain can overcome extended periods of E/I imbalance, potentially by processes that occur offline. The reactivation of mechanisms typically employed during juvenile learning, including night replay and activation of MHC I and microglia, could facilitate the recovery process following perturbation in the adult brain. This indicates that some forms of circuit plasticity may persist throughout adulthood, entering a dormant state until their activation is required for circuit restoration.

Methods

Animals

All procedures involving zebra finches were approved by the Institutional Animal Care and Use Committee of the California Institute of Technology. All birds used in the current study were bred in our own colony and housed with multiple conspecific cage mates of mixed genders and ages until used for experiments. Before any experiments, adult male birds (>120 days post-hatching (dph)) were singly housed in sound isolation cages with a 14/10 hr light/dark cycle for >5 days until they habituated to the new environment and started singing. Thereafter, birds were kept in isolation until the end of the experiment.

Behavioral recordings

Adult male zebra finches' (n=30, 130-890 dph) undirected songs were recorded 24/7 in sound-isolated chambers for 10-14 days before any manipulation to get a baseline of their song. Recordings were done with microphones (Audio-technica, AT831b) that are connected to an amplifier M-TRACK 8 and recording software Sound Analysis Pro 2011 at 44100 Hz. Animals were housed in these chambers and continuously recorded for the duration of the experiments.

Viral vectors

AAV-TeNT contained the promoter from the human dlx5 gene driving expression of the light chain of tetanus toxin fused to EGFP with a PEST domain. AAV9-dlx-TeNT was obtained from the Duke viral core facility. The control virus used was AAV9-CAG-NeonGreen, where CAG drives the expression of NeonGreen which is a GFP variant.

Stereotaxic injection

Birds were anesthetized with isoflurane (0.5% for initial induction, 0.2% for maintenance) and head-fixed on a stereotaxic apparatus. First, to inject a retrograde tracer in area X, craniotomies were made bilaterally and fluorescent tracers (fluoro-ruby 10%, 100-300 nL) were injected through a glass capillary (tip size ~25 µm) into the corresponding nuclei (coordinates from dorsal sinus in mm - area X: Anteroposterior (AP) 3.3-4.2, Mediolateral (ML) 1.5-1.6, Deep (D): 3.5-3.8). To deliver the virus (AAV) into HVC, a second surgery was performed 7-10 days after retrograde tracer injection. By then, HVC was strongly labeled by fluorescence and visible through a fluorescent stereoscope. AAVs diffuse extensively (~500 µm), and a single injection (~100 nL) in the center of HVC was sufficient to label enough cells. All injections in HVC were performed at ~20 nL/min to minimize physical damage. At the end of every surgery, craniotomies were covered with Kwik-Sil, and the skin incision was closed with Gluture.

Chronic electrophysiology recordings

Animals (n=4, 300-700 dph) were implanted in the right hemisphere HVC with 4 by 4 electrode arrays (Neuronexus A4x4-3mm-50/100-125-703-CM16LP) based on retrograde fluorescent labeling of HVC (just as for viral injections). Post-perfusion histology images were obtained to locate the electrode array within HVC for each animal (Supplementary Figure 15). Electrode implantation occurred within the same surgery as the viral injection.

This procedure follows the same surgical steps as the viral delivery protocol, until the point of electrode implantation. A small opening was cut on the dura (just big enough to fit the electrode array) to lower the electrodes manually. The reference and ground were a gold screw pin placed into the cerebellum. The skin was removed from the surface of the skull for the majority of the surface, in order to secure the implant. Before implantation, the skull and the craniotomies were cleaned with saline and dried and the skull was prepared according to the protocol of the C&B Metabond cement system. Post implantation we covered the craniotomies with kwik-sil. Once hardened, we covered the whole skull, and the part of the electrode still exposed, with metabond. The head stage (Intan RHD Part # C3335) was connected to the probe before implantation and securely metabonded to the connection between the probe and head stage in order to prevent detachment when the bird is moving. SPI interface cables (Intan Part #C3203, #C3213) were connected to the acquisition board (Open Ephys). Data was recorded at 30,000 Hz with the Open Ephys software system. Animals were freely moving with a passive counterweight-based commitator system.

Acute electrophysical recordings

Animals (n=10, 140-250 dph) went through the same surgical procedure as described for a stereotaxic viral injection. However, at the end of the surgery the skin was removed from the skull, and the whole skull was pre-treated and covered in metabond except for the craniotomies over HVC that were covered with kwik-cast until the day of the acute recording session. Shortly before the recording session, a head-bar was glued on top of the frontal surface of the metabonded skull to allow the head-fixation of the bird

for the recording session. Then, the kwik-cast was removed from the craniotomy over HVC (left or right hemisphere or both depending on the animal) and a small incision was made in the dure over HVC, which was identified by the retrograde tracer previously injected. The ground was placed into the cerebellum. Then the high-density silicone probe (Neuropixel) was lowered with a motorized arm over hours for 2.6-3 mm deep into the brain. The head stage and acquisition board was connected to the computer and data was recorded with the Open Ephys software. Once the probe settled in the brain, we had 4 distinct recording sessions. Post-perfusion histology images were obtained to locate electrode array within HVC for each animal (Supplementary Figure 16). Recording sessions: lights on silence (10 min), followed by playback of the bird's own song (3-10 min); lights-off silence (10 min), followed by playback of the bird's own song (3-10 min); microinjection of 100 nL 250 µM Gabazine (Hellobio, HB0901), followed by the same protocol of lights-off and on without Gabazine.

Song analysis

Song analysis was performed using MATLAB (MathWorks).

Song feature parameterization

Continuous audio recordings (44.1 kHz) were segmented into individual bouts manually. We used the open-source Matlab software package, Sound Analysis Pro 201 [41] to generate spectrograms and derive non-linear, time-varying song parameterizations. The time-varying features were: pitch, goodness of pitch, Wiener entropy, log-power of the spectrogram, mean frequency, and the maximum power in each quadrant of the frequency range 0- 11 kHz (labeled power 1, power 2, power 3, and power 4). These features were computed across the entire bout every 1 ms. These time-varying features were the base from which various portions of the song were further characterized.

Syllable parameterization

To quantify the change in the acoustic structure of the song, we tracked song features over the course of the perturbation. In Fig 1, we took the average feature values over all song segments in the three closest days of recorded song for each day plotted. We extracted the average mean frequency, average pitch, maximum goodness of pitch, maximum log power, minimum entropy, and entropy variance over the first 50 ms of each song segment, or the entire song segment if the segment was less than 50 ms. We centered and normalized feature values by the mean and standard deviation of the distribution of feature values in syllables five days pre-perturbation to compare trends across birds.

To visualize how the population of song segments evolved relative to the original syllable structure (Fig 1B), we plotted song segments as points in the first 2 principal components of the 7-dimensional acoustic feature space composed of: average mean frequency, average pitch, maximum goodness of pitch, maximum log power, minimum entropy, and entropy variance over the first 50 ms of each song segment, and the full duration of each song segment. 500 syllables recorded pre-perturbation were labeled by hand, and contour plots were made at the mean of each labeled stereotyped syllable type for visual reference

as the song degrades and recovers. Principal component dimensions were computed on the 500 labeled syllables, and subsequent song segments were projected into this principal component space.

Syllable segmentation

We identified syllables and silences within each bout by imposing thresholds on the time-varying, total log-power of the spectrogram. We selected the threshold based on manual inspection for each bird. We then performed a smoothing step wherein periods of silence less than 15 ms were converted to song segments. Song segments less than 20 ms were excluded from the analysis. Segmentation was further checked by eye by random sampling across both stereotyped motifs and degraded song. We then applied the power threshold to the entire course of song recordings for each bird.

A note on terminology: we refer to song segments to indicate continuous periods of singing. In the unperturbed song, these song segments are termed syllables. Because this is a continuous recovery process, these terms sometimes overlap in our usage.

Syllable timing distributions

Syllable durations were extracted from the syllable segmentation process. Discrete distributions of syllable durations were computed by normalizing each distribution of all song segment durations within individual days such that the sum of each daily distribution over all binned durations equaled one. Distributions for individual days were then assembled into a matrix wherein the columns represented normalized distributions for individual days. This matrix was plotted as a heat map in Supplementary Figure 1.

Continuous representation of bout trajectory

We generated continuous visualizations of bouts across the entire perturbation trajectory as shown in the graphical abstract [42,43]. We randomly sampled 100 bouts from single days of recording to build a representative sample of the song over the course of the experiment. For each bout, we slid a 150 ms window in 3 ms steps along the bout length. We then generated a high-dimensional, acoustic parameterization of each 150 ms song window by taking the moving average in 20 ms segments every 5 ms of six song features (mean frequency, pitch, goodness of pitch, power 4, power 2, and summed log power of the spectrogram). We performed principal component analysis on this high-dimensional set across all bouts to reduce the feature set to 30 dimensions.

Analysis of the chronic electrophysiology recordings

Preprocessing of Data

Bad channels were removed from analysis by visual inspection of the first minute of each recording. Three of the four birds studied had one channel that had behavior that was an order of magnitudes larger than all others and data from this channel was removed for further analysis.

Detection of sharp waves

Accelerometer and electrophysiology data were resampled to 125 Hz from the original 30,000 Hz using the Matlab resample function. Since accelerometer data was not zero-centered, the mean was subtracted before resampling and then added back to avoid edge effects from the lowpass filtering during resampling. Sharp waves were detected from the downsampled data using a procedure adapted from a zebra finch sleep study [44] and were only detected during periods of low movement. This was determined by setting a threshold on the moving standard deviation of the velocity as movement events appeared as large fluctuations in the velocity data. Briefly, the local field potential (LFP) traces were averaged across all electrodes and bandpassed from 1 to 40 Hz using MATLAB's bandpass function. Putative events were detected by peaks in the inverted (-1x) trace and were in the lowest 5% of all values during non-movement, were at least 10 ms long, and were 80 ms apart. These putative events were used to construct a template by taking the average 80 ms trace centered on each event. Cross-correlating this template with the entire overnight LFP trace and taking the z- score (mean and SD from only non-movement times) revealed events that closely matched the template. Peaks were detected in the z-scored cross-correlation and defined as events if they were above a given threshold and were at least 80 ms apart. Notably, thresholds were not tuned across birds or recordings but a constant threshold was sufficient in all birds to detect events. Extraction of sharp waves. The detected events were used to index the original 30,000 Hz data. 500 ms of data was extracted for each event and recentered on the minimal value in the center 100 ms. An equal number of 500 ms non-sharp wave events were extracted from a random selection of times without movement or sharp waves. Sharp waves with clear electrical noise were omitted from further analysis.

Multi-unit activity (MUA)

MUA was detected using an established method [45]. Briefly, channels were common averaged referenced, bandpassed from 600 to 6,000 Hz, and upsampled to 50,000 Hz. The square root of the local energy operator (Mukhopadhyay & Ray, 1998) was taken and then Gaussian smoothed ($\sigma = 0.4$). Thresholding this trace and then downsampling back to 30,000 Hz gave the times of high MUA.

Time-frequency analysis

The continuous wavelet transform was used to compute the spectra for each sharp wave. Percent increase relative to mean power spectra were averaged within each day and bird. The spectrum of average power in the center 33 ms of each event was used to compute the percent increase in power relative to non-sharp wave events at each frequency. To determine the presence of phase-amplitude coupling between low-frequency (10-20 Hz) and gamma-frequency (30-40Hz) bursts, the phase of the low-frequency band, and power of the high-frequency band were extracted using the Hilbert transform of the band-passed signal. Determining whether the peak gamma activity occurred at a consistent phase of the low-frequency oscillation, could suggest phase-amplitude coupling. To further assess this, we asked at what time and frequency a max in the spectrum occurred for each event, relative to the minima of each sharp wave. We also wanted to ask whether the power of deflections in different frequency bands differed significantly across control and experimental birds. We computed the relative increase in power in the frequency bands

of interest (15-30 Hz, and 30-70 Hz) during a deflection relative to non-deflection times. We then used a t-test to statistically test whether power differed significantly across birds for a given day.

Analysis of the acute electrophysiology recordings

The low-frequency electrophysiology data was recorded at 2,500 Hz while the high-frequency data was recorded at 30,000 Hz. A MATLAB script was written to analyze the low- and high-frequency oscillations. All low-frequency data was high pass filtered (1-300 Hz) and median subtracted. All high-frequency data was common average referenced and low-pass filtered (300-7,000 Hz). For deflection event detection, we used two methods. One to use a template per animal for extraction of deflection and non-deflection events with template matching in a semi-automated manner. Second, manually picked out peaks that were 9 standard deviations away from the average raw signal, then further manually curated these events. Most of our further analysis was done using the deflection events that resulted from template matching (except Supplementary Figure 10A for the difference in power between deflection and non-deflection event calculation). For spike detection, we used two separate methods, one to threshold the high-frequency data to only consider spikes that are 9 standard deviations above the average signal in a 2-minute window. The second method used for spike detection was using the Kilosort software v2.5 [46] to extract spikes from the raw data. Next, we manually curated the dataset to capture the waveform and firing rate of neurons. The thresholded spiking data was used to generate Figure 3BC. We performed statistics (Wilcoxon, rank sum test) to show statistically significant firing rates related to control in HVC and RA in Figure 3B.

To calculate the power difference between deflection and non-deflection events in the acute recording in Supplementary Figure 11 A, we used a script developed for the chronic recordings with the use of the built-in MATLAB function *pwelch*. To analyze the spectral decomposition of the LFP signature (Figure 3D) in control and TeNT-treated animals during the experimental timeline we calculated the Morse continuous wavelet transform using the built-in MATLAB function. From this finding, we obtained the mean oscillation at the alpha range (1-10 Hz) and at low gamma (30-70 Hz). Then, we performed an iterative alignment process of these two oscillations and calculated the angle of the low-frequency oscillation (from obtaining the Hilbert transform) at the peak amplitude of the high-frequency oscillation (Supplementary Figure 11BC). Then we proceeded to align the single neuronal firing (obtained from Kilosort) to the alpha and the low gamma oscillations and plotted the normalized probability distribution (Figure 3F) of neurons firing at a specific phase (angle) of the alpha or low gamma oscillations. We performed the Kolgomorov-Smirnov test on the cumulative density function (CDF) (Supplementary Figure 11D) to assess if the change in probability distribution in the relationship between alpha and low gamma oscillations is statistically significant from control distributions at 3-6, 20, and 70 dpi.

Single-cell RNA sequencing

Animals

All of the work described in this study was approved by California Institute of Technology and Oregon Health & Science University's Institutional Animal Care and Use Committee and is in accordance with

NIH guidelines. Zebra finches (Taeniopygia guttata) were obtained from our own breeding colony or purchased from local breeders.

Dissociation and cDNA generation

Animals were anesthetized with a mix of ketamine-xylazine (0.02 mL / 1 gram) and quickly decapitated, then the brain was placed into a carbogenated (95% O2, 5% CO2) NMDG-ACSF petri dish on ice. The brains were dissected on a petri dish with NMDG-ACSF surrounded by ice under an epifluorescent microscope guided by the fluoro-ruby retrograde tracing from Area X to HVC.

We used the commercially available Worthington Papain Dissociation system with some minor changes and add-on steps. We followed all the steps included in the Worthington protocol with a final concentration of 50 U/mL of papain. To match the intrinsic osmolarity of neurons in zebra finches we used NMDG-ACSF (~310 mOsm) instead of the EBSS for post-dissection and STOP solution. Another modification was to add 20 µL of 1 mg/mL Actinomycin D (personal communication from Allan-Hermann Pool; [47]) into 1 mL of the post-dissection medium and the STOP solution in which trituration occurred. Papain digestion occurred for an hour on a rocking surface with constant carbogenation in a secondary container above the sample vial at RT. We performed trituration with increasingly smaller diameter glass pasteur pipettes. Trituation was performed inside the papain solution. Then, once the tissue was fully dissociated, we centrifuged the samples at 300 g RT for 5 minutes and resuspended them in STOP solution. Next, we used a 40 µm Falcon cell strainer pre-wet with the STOP solution and centrifuged again at 300 g RT for 5 min. Finally, we resuspended the cell pellet in 60µl of STOP solution and proceeded to barcoding and cDNA synthesis. The cell barcoding, cDNA synthesis, and library generation protocol were performed according to the Chromium v3.1 next GEM single cell 3' reagent kits by Jeff Park in the Caltech sequencing facility. Sequencing was performed on an Illumina Novaseq S4 sequencer with 2x150 bp reads.

Generation of count matrices

The reference genome GCA_003957565.2 (Black17, no W) was retrieved from Ensembl on March 20, 2021 (http://ftp.ensembl.org/pub/release-104/gtf/taeniopygia_guttata/). We quantified the gene expression in each of the four datasets using the kallisto-bustools workflow [48]. The reference index was built using the kb-python (v0.26.3) *ref* command and the above-mentioned reference genome. Subsequently, the WRE sequence was manually added to the cdna and t2g files generated by kallisto-bustools to allow the identification of transgenic cells. The count matrix was generated for each dataset using the kallisto-bustools *count* function. The resulting count matrices were compared to those generated by the 10X Cell Ranger pipeline (v6.0.1) and kallisto-bustools *count* with *multimapping* function. For all four datasets, kallisto-bustools mapped approximately 10% more reads than Cell Ranger (Supplementary Figure 17). No increase in confidently mapped reads was observed when using the multimapping function, indicating that reads align confidently to one gene in the reference genome (Supplementary Figure 17).

Quality control and filtering

The datasets were filtered separately based on the expected number of cells and their corresponding minimum number of UMI counts (Supplementary Figure 11). Following quality control based on apoptosis markers and library saturation plots (Supplementary Figure 11), the count matrices were concatenated and normalized using log(CP10k + 1) for downstream dimensionality reduction and visualization using Scanpy's (v1.9.1; [49]) *normalize_total* with target sum 10,000 and *log1p*. Gene names and descriptions for Ensembl IDs without annotations were obtained using gget (v0.27.3; [50]).

Dimensionality reduction and normalization

The concatenated data was mapped to a lower dimensional space by PCA applied to the log-normalized counts filtered for highly variable genes using Scanpy's *highly_variable_genes*. Next, we computed nearest neighbors and conducted Leiden clustering [51] using Scanpy.

Initially, this approach was performed on the control and TeNT datasets separately. This resulted in the identification of 19 clusters in the control data and 22 clusters in the TeNT data (Supplementary Figure 11). For both conditions, equal contribution from both datasets indicated that there was minimal batch effect, as expected since the data was sequenced in a pooled sequencing run. We also performed batch correction using scVI [52] which did not change the contribution of each dataset per cluster. As a result, we continued the analysis using the data that was not batch-corrected with scVI.

Next, we concatenated all four datasets and followed the approach described above. This resulted in the identification of 21 Leiden clusters, which we also refer to as cell types (Figure 4 A). Each cluster was manually annotated with a cell type based on the expression of previously established marker genes [53]. The cell type annotation was validated by the top 20 differentially expressed genes extracted from each cluster using Scanpy's rank_genes_groups (P values were computed using a t-test and adjusted with the Bonferroni method for multiple testing) (Supplementary Figure 12). Clusters identified as glutamatergic neurons were further broken down into HVC-X- and HVC-RA-projecting glutamatergic neurons using previously established marker genes (data not shown; also see https://github.com/lauraluebbert/TL_2023). We found that reclustering all cells labeled as glutamatergic neurons using the Leiden algorithm did not yield different results and we therefore continued with the initial clusters (data not shown). All results discussed in this paper were confirmed by both jointly and separately clustering the experimental conditions.

Comparative analysis of clusters and conditions

Differentially expressed genes between clusters were identified using Scanpy's *rank_genes_groups* (p values were computed using a t-test and adjusted with the Bonferroni method for multiple testing, and confirmed by comparison to P values generated with Wilcoxon test with Bonferroni correction). In the violin plots, unless otherwise indicated, a star indicates a p value < 0.05 and a fold change > 1.5 difference in mean gene expression between the indicated conditions (p value computed with scipy.stats' (v1.7.0) *ttest_ind* and adjusted with the Bonferroni method for multiple testing).

In situ hybridization

Animals

All of the work described in this study was approved by the California Institute of Technology and Oregon Health & Science University's Institutional Animal Care and Use Committee and is in accordance with NIH guidelines. Zebra finches (Taeniopygia guttata) were obtained from our own breeding colony or purchased from local breeders. Developmental gene expression in HVC in the 20-, 50-, and 75-days post-hatch (dph) male and female zebra finches was assessed as previously described [54]. The sex of birds was determined by plumage and gonadal inspection. Birds were sacrificed by decapitation, bisected in the sagittal plane and flash-frozen in Tissue-Tek OCT (Sakura-Finetek), and frozen in a dry ice/isopropyl alcohol slurry. Brains of TeNT-manipulated finches were coronally blocked anterior to the tectum and flash frozen in Tissue-Tek (Sakura). All brains were sectioned at 10um on a cryostat and mounted onto charged slides (Superfrost Plus, Fisher).

In situ hybridization

In situ hybridization was performed as previously described [55,56]. Briefly, DIG-labeled riboprobes were synthesized from cDNA clones for RGS10 (CK312091) and LOC100231469 (class I histocompatibility antigen, F10 alpha chain; DV951963). Slides containing the core of HVC were hybridized overnight at 65°C. Following high stringency washes, sections were blocked for 30 min and then incubated in an alkaline phosphatase conjugated anti-DIG antibody (1:600, Roche). Slides were then washed and developed overnight in BCIP/NBT chromogen (Perkin Elmer). To minimize experimental confounds between animals, sections for each gene were fixed together in 3% paraformaldehyde, hybridized with the same batch of probe, and incubated in chromogen for the same duration.

Sections were imaged under consistent conditions on a Nikon E600 microscope with a Lumina HR camera and imported into ImageJ for analysis. We quantified the expression level of the gene as measured by optical density and the number of cells expressing the gene per unit area, as previously described [54]. Optical density was measured by taking the average pixel intensity of a 300x300 pixel square placed over the center of HVC. This value was normalized to the average background level of the tissue. To quantify the number of labeled cells, we established a threshold of expression that was 2.5x the background level. Binary filters (Close-, Open) were applied and the number of particles in the same 300x300 pixel square was quantified.

Histology

After cardiac perfusion with room temperature 3.2% PFA in 1xPBS we let the brains fix for 2-4 hours at room temperature. After each hemisphere of the brain was sectioned sagittally with a vibratome at 70-100 µm thickness. The brain slices containing HVC were collected and incubated at 4 C overnight with the primary rabbit anti-GFP (AB3080P, EMD Milipore) (blocked in 10% donkey serum in 0.2% Triton 1xPBS). On the second day, the brains were washed in 0.05% Triton 1xPBS and incubated for 2 hours in the dark at room temperature in the secondary goat anti-rabbit 488 (ab150077). Next, the brain slices were washed and mounted in Fluoromount (Sigma). Confocal images were taken with the LSM800.

Data and Code Availability

Data generated in this study have been deposited in Caltech DATA and can be found at the following DOIs: https://doi.org/10.22002/ednra-nn006 and https://doi.org/10.22002/3ta8v-gj982. Please do not hesitate to contact the authors for data or code requests. The code used for the analysis of the single-cell RNA sequencing data can be found here: https://github.com/lauraluebbert/TL_2023. The code used for the analysis of the chronic electrophysiology data can be found here: https://github.com/jordan-feldman/Torok2023-ephys.

Author contributions

Conceived the ideas of experimental design of the study – ZT, CL
Perform behavioral, single-cell, and electrophysiology experiments/ data collection – ZT
Perform molecular or imaging experiments/ data collection – ZT, LL, SW, AAN, JP (from methods)
Data analysis and interpretation – ZT, LL, JF, AD, WG
Manuscript writing – ZT, LL, CL
Stylistic/grammatical revisions – ZT, LL, AD, AF, CVM, LP
Provided revisions to scientific content of manuscript - LL, JF, AD, AAN, CVM, AF, LP, WG, CL
Provided funding – AF, LP, CL

Acknowledgements

Funding source: R01NS104925A, Caltech BBE department, Chen Innovator Grant 2019
We thank Jeff Park and the Caltech Sequencing Facility for the library generation.
We thank Daniel Pollak for early chronic electrophysiology advice and Allan Hermann-Pool for advice on the single-cell RNA sequencing experimental pipeline.

Declaration of Interests

The authors declare no competing interests.

References

1. Dehghani, N., Peyrache, A., Telenczuk, B., Le Van Quyen, M., Halgren, E., Cash, S.S., Hatsopoulos, N.G., and Destexhe, A. (2016). Dynamic Balance of Excitation and Inhibition in Human and Monkey Neocortex. Sci. Rep. *6*, 23176.

2. Fritschy, J.-M. (2008). Epilepsy, E/I balance and GABA(A) receptor plasticity. Front. Mol. Neurosci. *1*, 5.

3. Cossart, R., Bernard, C., and Ben-Ari, Y. (2005). Multiple facets of GABAergic neurons and synapses: multiple fates of GABA signalling in epilepsies. Trends Neurosci. *28*, 108–115.

4. Nottebohm, F., Stokes, T.M., and Leonard, C.M. (1976). Central control of song in the canary, Serinus canarius. J. Comp. Neurol. *165*, 457–486.

5. Kozhevnikov, A.A., and Fee, M.S. (2007). Singing-related activity of identified HVC neurons in the zebra finch. J. Neurophysiol. *97*, 4271–4283.

6. Brainard, M.S., and Doupe, A.J. (2002). What songbirds teach us about learning. Nature *417*, 351–358.

7. Vallentin, D., Kosche, G., Lipkind, D., and Long, M.A. (2016). Neural circuits. Inhibition protects acquired song segments during vocal learning in zebra finches. Science *351*, 267–271.

8. Kosche, G., Vallentin, D., and Long, M.A. (2015). Interplay of inhibition and excitation shapes a premotor neural sequence. J. Neurosci. *35*, 1217–1227.

9. Dimidschstein, J., Chen, Q., Tremblay, R., Rogers, S.L., Saldi, G.-A., Guo, L., Xu, Q., Liu, R., Lu, C., Chu, J., et al. (2016). A viral strategy for targeting and manipulating interneurons across vertebrate species. Nat. Neurosci. *19*, 1743–1749.

10. Link, E., Edelmann, L., Chou, J.H., Binz, T., Yamasaki, S., Eisel, U., Baumert, M., Südhof, T.C., Niemann, H., and Jahn, R. (1992). Tetanus toxin action: inhibition of neurotransmitter release linked to synaptobrevin proteolysis. Biochem. Biophys. Res. Commun. *189*, 1017–1023.

11. Vu, E.T., Mazurek, M.E., and Kuo, Y.C. (1994). Identification of a forebrain motor programming network for the learned song of zebra finches. J. Neurosci. *14*, 6924–6934.

12. Yu, A.C., and Margoliash, D. (1996). Temporal hierarchical control of singing in birds. Science *273*, 1871–1875.

13. Glaze, C.M., and Troyer, T.W. (2006). Temporal structure in zebra finch song: implications for motor coding. J. Neurosci. *26*, 991–1005.

14. Brainard, M.S., and Doupe, A.J. (2000). Interruption of a basal ganglia–forebrain circuit prevents plasticity of learned vocalizations. Nature *404*, 762–766.

15. Olveczky, B.P., Andalman, A.S., and Fee, M.S. (2005). Vocal experimentation in the juvenile songbird requires a basal ganglia circuit. PLoS Biol. *3*, e153.

16. Kao, M.H., Doupe, A.J., and Brainard, M.S. (2005). Contributions of an avian basal ganglia–forebrain circuit to real-time modulation of song. Nature *433*, 638–643.

17. Markowitz, J.E., Liberti, W.A., 3rd, Guitchounts, G., Velho, T., Lois, C., and Gardner, T.J. (2015). Mesoscopic patterns of neural activity support songbird cortical sequences. PLoS Biol. *13*, e1002158.

18. Brown, D.E., 2nd, Chavez, J.I., Nguyen, D.H., Kadwory, A., Voytek, B., Arneodo, E.M., Gentner, T.Q., and Gilja, V. (2021). Local field potentials in a pre-motor region predict learned vocal sequences. PLoS Comput. Biol. *17*, e1008100.

19. Crandall, S.R., Adam, M., Kinnischtzke, A.K., and Nick, T.A. (2007). HVC neural sleep activity increases with development and parallels nightly changes in song behavior. J. Neurophysiol. *98*, 232–240.

20. Dave, A.S., and Margoliash, D. (2000). Song replay during sleep and computational rules for sensorimotor vocal learning. Science *290*, 812–816.

21. Elmaleh, M., Kranz, D., Asensio, A.C., Moll, F.W., and Long, M.A. (2021). Sleep replay reveals premotor circuit structure for a skilled behavior. Neuron *109*, 3851–3861.e4.

22. Hahnloser, R.H.R., Kozhevnikov, A.A., and Fee, M.S. (2006). Sleep-related neural activity in a premotor and a basal-ganglia pathway of the songbird. J. Neurophysiol. *96*, 794–812.

23. Shank, S.S., and Margoliash, D. (2009). Sleep and sensorimotor integration during early vocal learning in a songbird. Nature *458*, 73–77.

24. Wang, B., Torok, Z., Duffy, A., Bell, D., Wongso, S., Velho, T., Fairhall, A., and Lois, C. (2022). Unsupervised Restoration of a Complex Learned Behavior After Large-Scale Neuronal Perturbation. bioRxiv, 2022.09.09.507372. 10.1101/2022.09.09.507372.

25. Jun, J.J., Steinmetz, N.A., Siegle, J.H., Denman, D.J., Bauza, M., Barbarits, B., Lee, A.K., Anastassiou, C.A., Andrei, A., Aydın, Ç., et al. (2017). Fully integrated silicon probes for high-density recording of neural activity. Nature *551*, 232–236.

26. Steinmetz, N.A., Koch, C., Harris, K.D., and Carandini, M. (2018). Challenges and opportunities for large-scale electrophysiology with Neuropixels probes. Curr. Opin. Neurobiol. *50*, 92–100.

27. Fisher, R.S., Scharfman, H.E., and deCurtis, M. (2014). How can we identify ictal and interictal abnormal activity? Adv. Exp. Med. Biol. *813*, 3–23.

28. Lubenov, E.V., and Siapas, A.G. (2009). Hippocampal theta oscillations are travelling waves. Nature *459*, 534–539.

29. Buzsáki, G. (1986). Hippocampal sharp waves: their origin and significance. Brain Res. *398*, 242–252.

30. Hulse, B.K., Lubenov, E.V., and Siapas, A.G. (2017). Brain State Dependence of Hippocampal Subthreshold Activity in Awake Mice. Cell Rep. *18*, 136–147.

31. Joo, H.R., and Frank, L.M. (2018). The hippocampal sharp wave–ripple in memory retrieval for immediate use and consolidation. Nat. Rev. Neurosci. *19*, 744–757.

32. Lenz, K.M., and Nelson, L.H. (2018). Microglia and Beyond: Innate Immune Cells As Regulators of Brain Development and Behavioral Function. Front. Immunol. *9*, 698.

33. Li, Q., and Barres, B.A. (2018). Microglia and macrophages in brain homeostasis and disease. Nat. Rev. Immunol. *18*, 225–242.

34. Thion, M.S., Ginhoux, F., and Garel, S. (2018). Microglia and early brain development: An intimate journey. Science *362*, 185–189.

35. Parkhurst, C.N., Yang, G., Ninan, I., Savas, J.N., Yates, J.R., 3rd, Lafaille, J.J., Hempstead, B.L., Littman, D.R., and Gan, W.-B. (2013). Microglia promote learning-dependent synapse formation through brain-derived neurotrophic factor. Cell *155*, 1596–1609.

36. Simpson, E. (1988). Function of the MHC. Immunol. Suppl. *1*, 27–30.

37. Elmer, B.M., and McAllister, A.K. (2012). Major histocompatibility complex class I proteins in brain development and plasticity. Trends Neurosci. *35*, 660–670.

38. Chacon, M.A., and Boulanger, L.M. (2013). MHC class I protein is expressed by neurons and neural progenitors in mid-gestation mouse brain. Mol. Cell. Neurosci. *52*, 117–127.

39. Shatz, C.J. (2009). MHC class I: an unexpected role in neuronal plasticity. Neuron *64*, 40–45.

40. Lazarczyk, M.J., Kemmler, J.E., Eyford, B.A., Short, J.A., Varghese, M., Sowa, A., Dickstein, D.R., Yuk, F.J., Puri, R., Biron, K.E., et al. (2016). Major Histocompatibility Complex class I proteins are critical for maintaining neuronal structural complexity in the aging brain. Sci. Rep. *6*, 26199.

41. Tchernichovski, O., Nottebohm, F., Ho, C.E., Pesaran, B., and Mitra, P.P. (2000). A procedure for an automated measurement of song similarity. Anim. Behav. *59*, 1167–1176.

42. Goffinet, J., Brudner, S., Mooney, R., and Pearson, J. (2021). Low-dimensional learned feature spaces quantify individual and group differences in vocal repertoires. Elife *10*. 10.7554/eLife.67855.

43. Sainburg, T., Thielk, M., and Gentner, T.Q. (2020). Finding, visualizing, and quantifying latent structure across diverse animal vocal repertoires. PLoS Comput. Biol. *16*, e1008228.

44. Yeganegi, H., Luksch, H., and Ondracek, J.M. (2019). Hippocampal-like network dynamics underlie avian sharp wave-ripples. bioRxiv, 825075. 10.1101/825075.

45. Shan, K.Q., Lubenov, E.V., and Siapas, A.G. (2017). Model-based spike sorting with a mixture of drifting t-distributions. J. Neurosci. Methods *288*, 82–98.

46. Pachitariu, M., Steinmetz, N., Kadir, S., Carandini, M., and Harris, K.D. (2016). Kilosort: realtime spike-sorting for extracellular electrophysiology with hundreds of channels. bioRxiv, 061481. 10.1101/061481.

47. Pool, A.-H., Wang, T., Stafford, D.A., Chance, R.K., Lee, S., Ngai, J., and Oka, Y. (2020). The cellular basis of distinct thirst modalities. Nature *588*, 112–117.

48. Melsted, P., Sina Booeshaghi, A., Gao, F., Beltrame, E., Lu, L., Hjorleifsson, K.E., Gehring, J., and Pachter, L. (2019). Modular and efficient pre-processing of single-cell RNA-seq. bioRxiv, 673285. 10.1101/673285.

49. Wolf, F.A., Angerer, P., and Theis, F.J. (2018). SCANPY: large-scale single-cell gene expression data analysis. Genome Biol. *19*, 15.

50. Luebbert, L., and Pachter, L. (2023). Efficient querying of genomic reference databases with gget. Bioinformatics *39*. 10.1093/bioinformatics/btac836.

51. Traag, V.A., Waltman, L., and van Eck, N.J. (2019). From Louvain to Leiden: guaranteeing well-connected communities. Sci. Rep. *9*, 5233.

52. Lopez, R., Regier, J., Cole, M.B., Jordan, M.I., and Yosef, N. (2018). Deep generative modeling for single-cell transcriptomics. Nat. Methods *15*, 1053–1058.

53. Colquitt, B.M., Merullo, D.P., Konopka, G., Roberts, T.F., and Brainard, M.S. (2021). Cellular transcriptomics reveals evolutionary identities of songbird vocal circuits. Science *371*. 10.1126/science.abd9704.

54. Zemel, B.M., Nevue, A.A., Dagostin, A., Lovell, P.V., Mello, C.V., and von Gersdorff, H. (2021). Resurgent Na+ currents promote ultrafast spiking in projection neurons that drive fine motor control. Nat. Commun. *12*, 6762.

55. Carleton, J.B., Lovell, P.V., McHugh, A., Marzulla, T., Horback, K.L., and Mello, C.V. (2014). An optimized protocol for high-throughput in situ hybridization of zebra finch brain. Cold Spring Harb. Protoc. *2014*, 1249–1258.

56. Nevue, A.A., Lovell, P.V., Wirthlin, M., and Mello, C.V. (2020). Molecular specializations of deep cortical layer analogs in songbirds. Sci. Rep. *10*, 18767.

Supplementary Figures

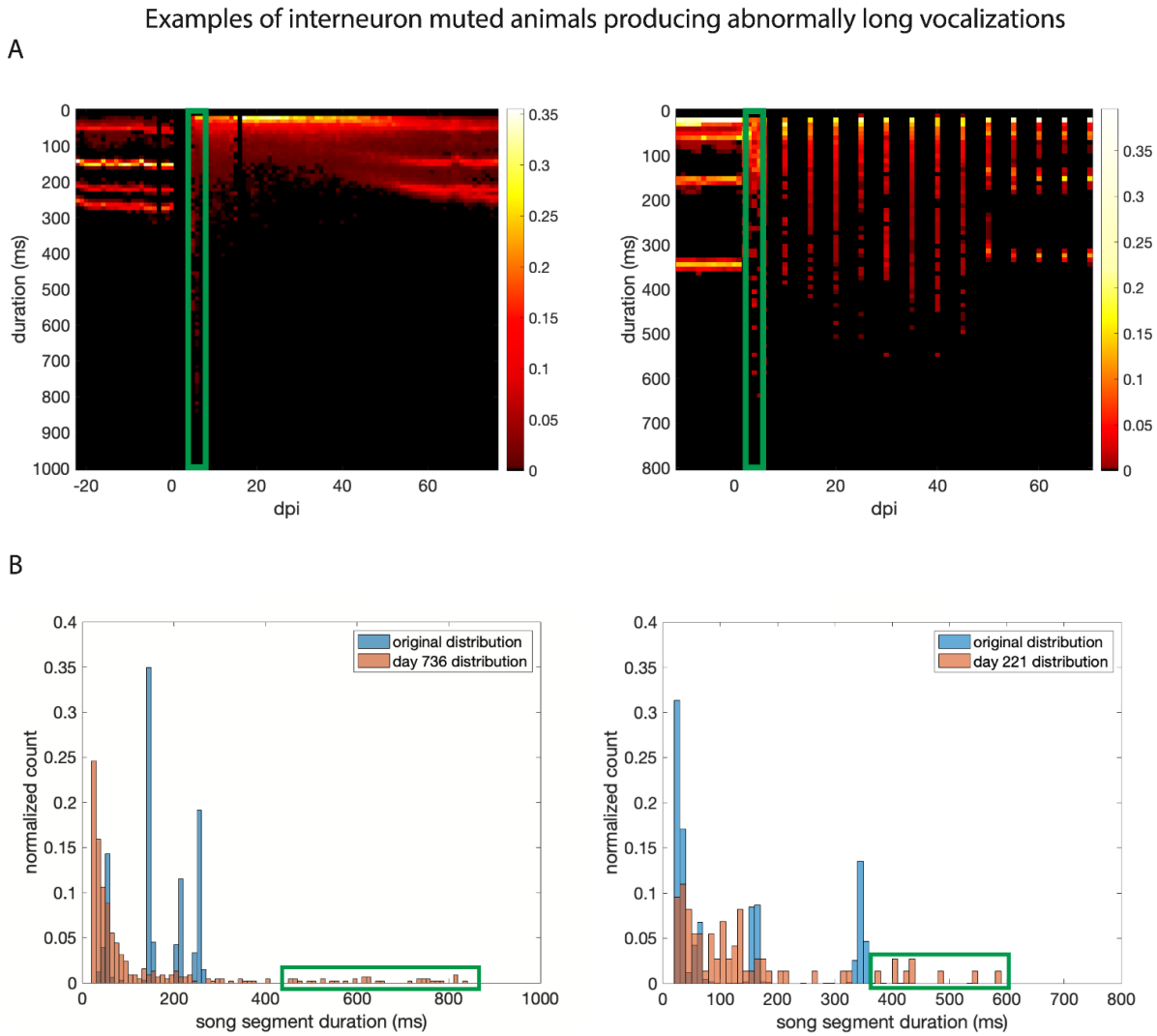

Supplementary Figure 1: *<u>Examples of abnormally long syllable lengths after injection of interneuron muting virus in two animals.</u>* ***A*** *Syllable length durations for the length of song degradation and recovery. The Y axis depicts the length of the syllables in milliseconds plotted over days post-injection (dpi) of either TeNT virus. TeNT-treated animals displayed a short period during which some vocalizations were of length not observed in normal animals and eventually became highly variable and shorter (shifts to shorter length sounds). The green rectangle highlights the day post-injection portrayed in B for each animal.* ***B*** *Histogram of syllable durations (blue trace is before injection of virus, orange trace is after injection of virus). The green rectangle highlights vocalizations of abnormal length.*

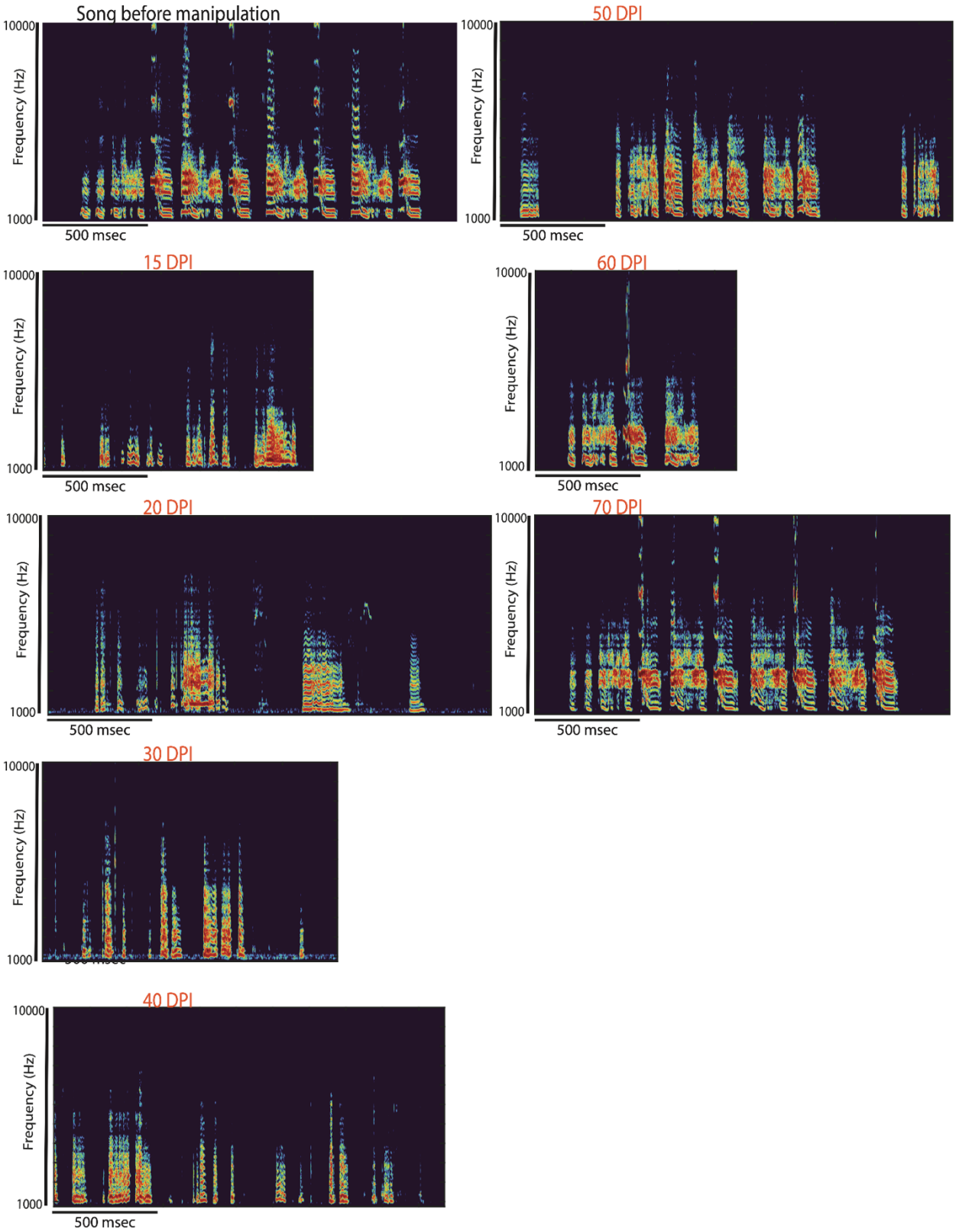

Figure legend on next page.

Supplementary Figure 2: *Example spectrograms of a TeNT-treated animal (B138) during song degradation and recovery. Vocalizations between 15 dpi and 30 dpi were much shorter than the first long syllables shown in Figure 1 A at 5 dpi.*

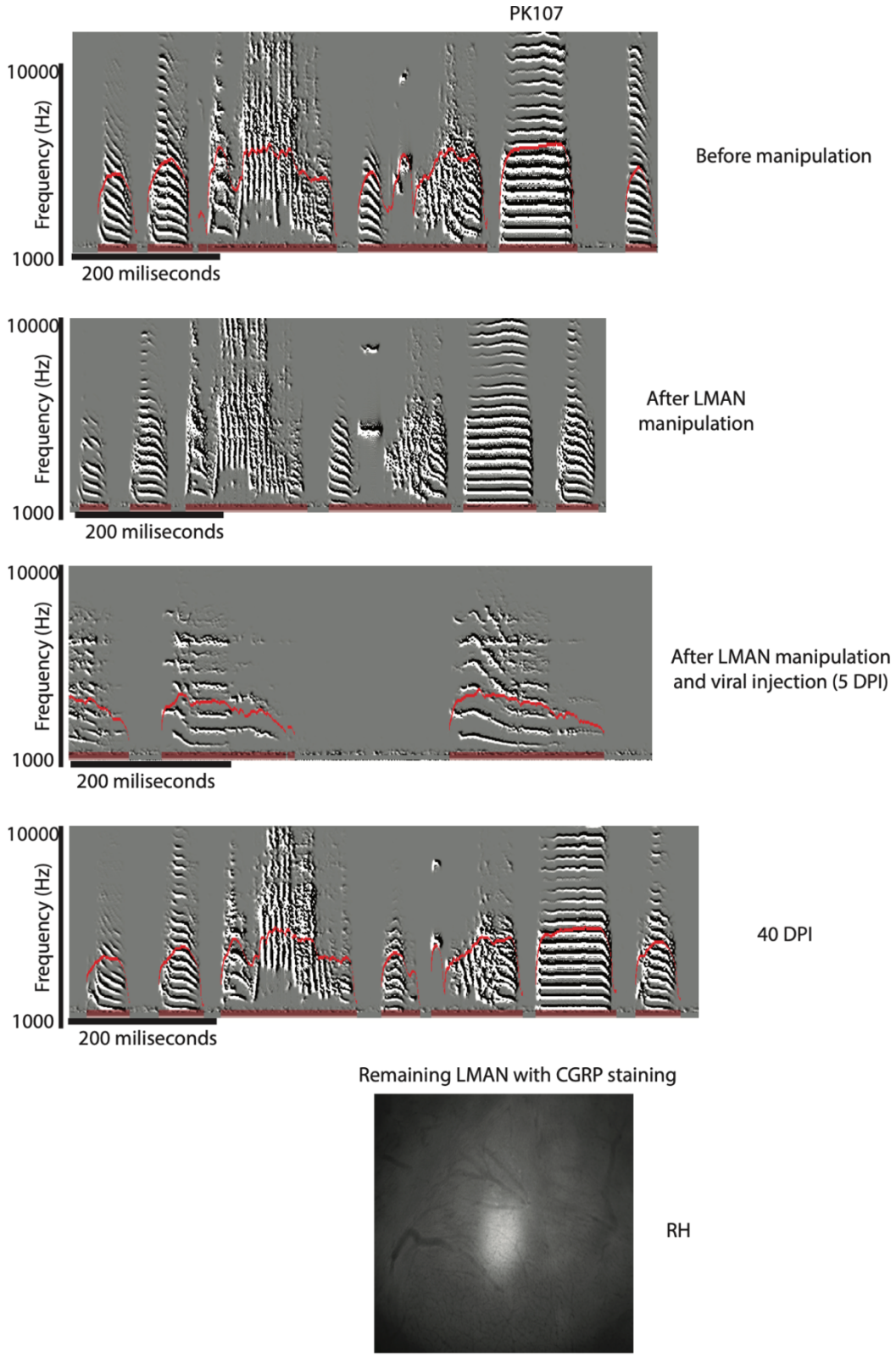

Figure legend on next page.

Supplementary Figure 3: *Song degradation and recovery after chronic removal of inhibition in an animal without LMAN. Spectrograms are showing the song of the animal before and after LMAN lesion at 5 and 40 days post viral injection (dpi). The histology image shows the amount of LMAN left (based on CGRP staining) in the right hemisphere (RH).*

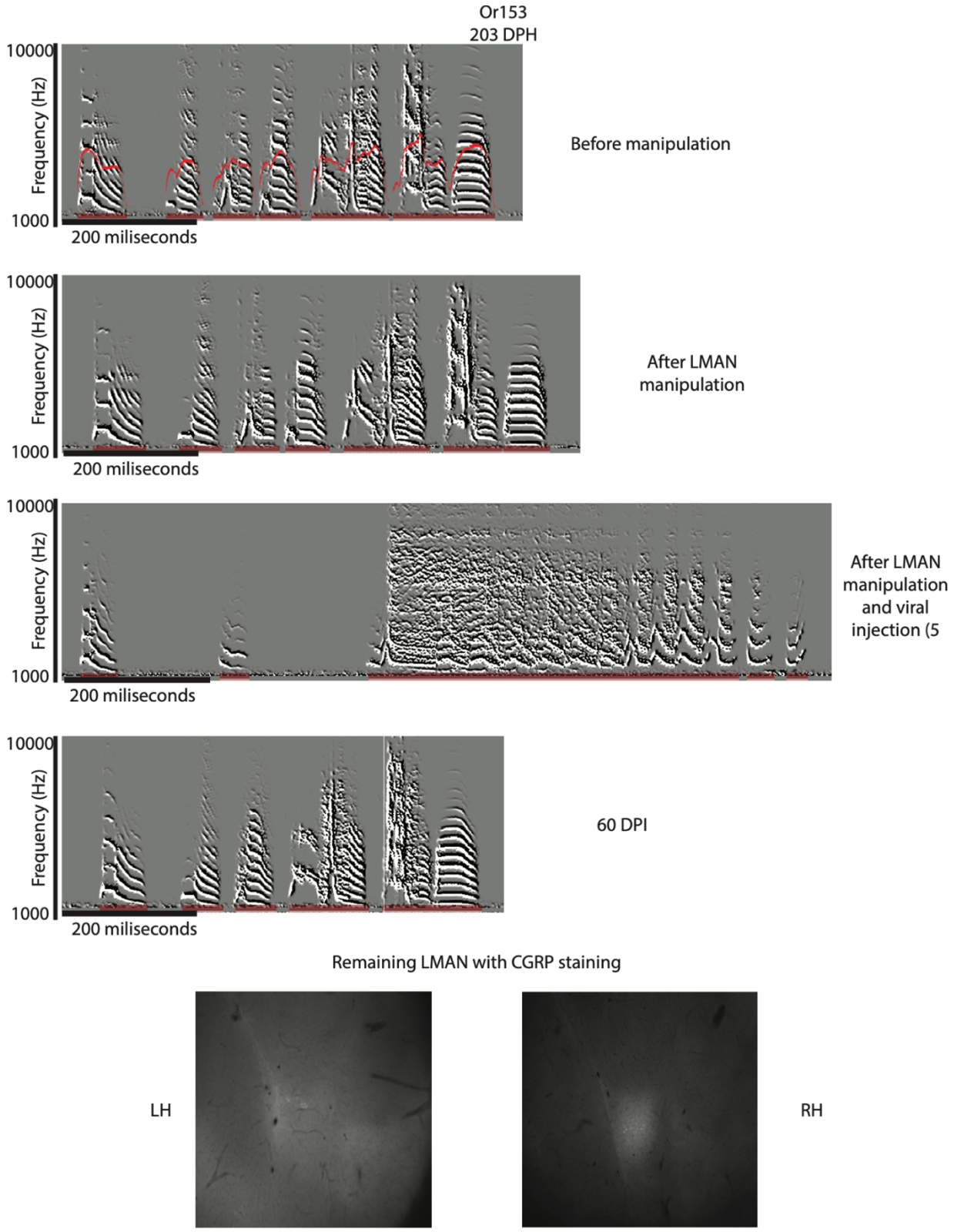

Figure legend on next page.

Supplementary Figure 4: *Song degradation and recovery after chronic removal of inhibition in an animal without LMAN. Spectrograms are showing the song of the animal before and after LMAN lesion at 5 and 60 days post viral injection (dpi). The histology images indicate the amount of LMAN left (based on CGRP staining) in the left (LH) and right (RH) hemispheres.*

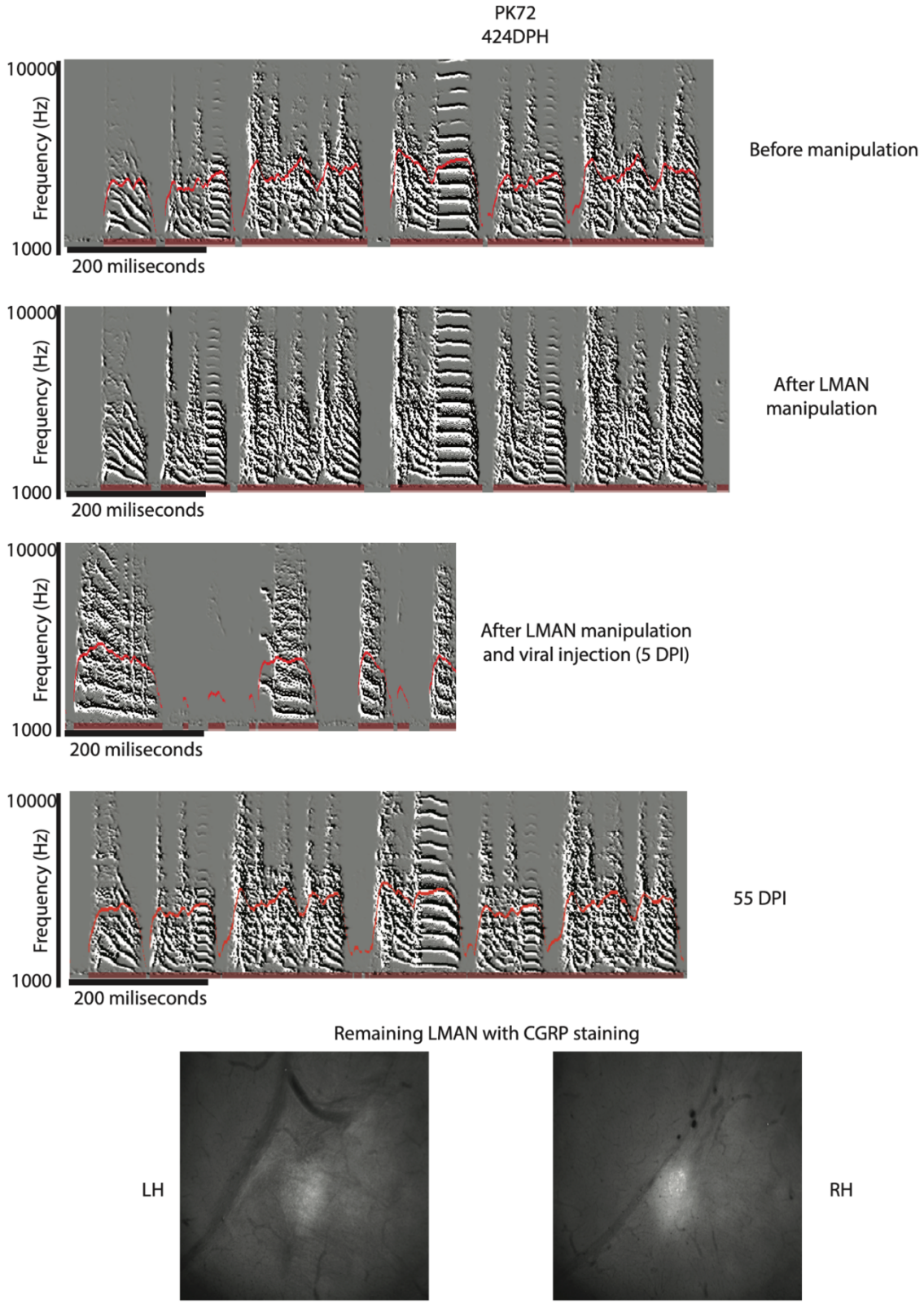

Figure legend on next page.

Supplementary Figure 5: *Song degradation and recovery after chronic removal of inhibition in an animal without LMAN. Spectrograms are showing the song of the animal before and after LMAN lesion at 5 and 55 days after viral injection (dpi). The histology images indicate the amount of LMAN left (based on CGRP staining) in the left (LH) and right (RH) hemispheres.*

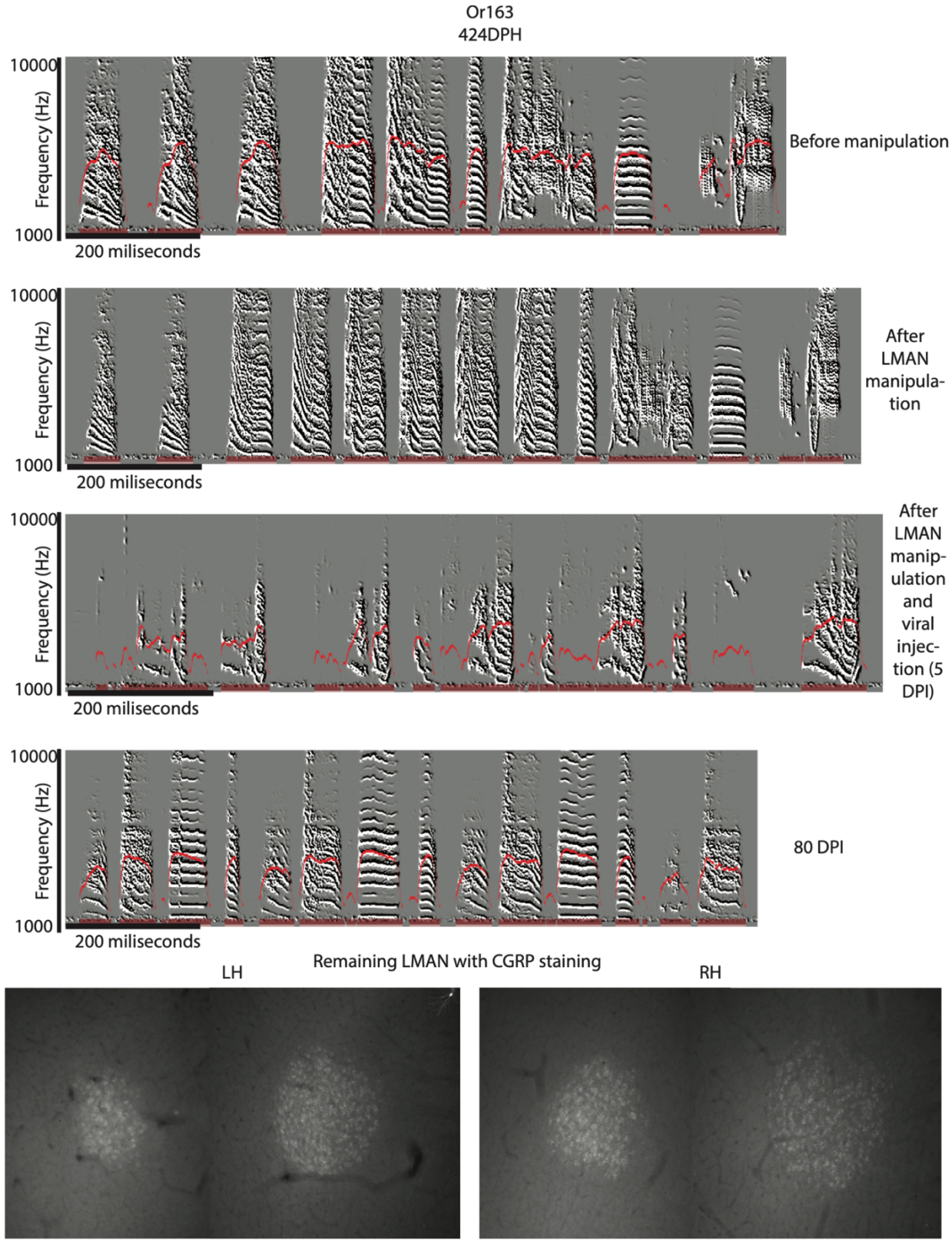

Figure legend on next page.

Supplementary Figure 6: *Song degradation and lack of recovery after chronic removal of inhibition in an animal without LMAN. Spectrograms showing the song of the animal before and after LMAN lesion at 5 and 40 days post-injection (dpi). The histology images indicate the amount of LMAN left (based on CGRP staining) in the left (LH) and right (RH) hemispheres. This animal represents a good example where, aside from having sustainable LMAN input, the song did not recover. This suggests that LMAN is not the driver of song degradation or recovery in this experimental paradigm.*

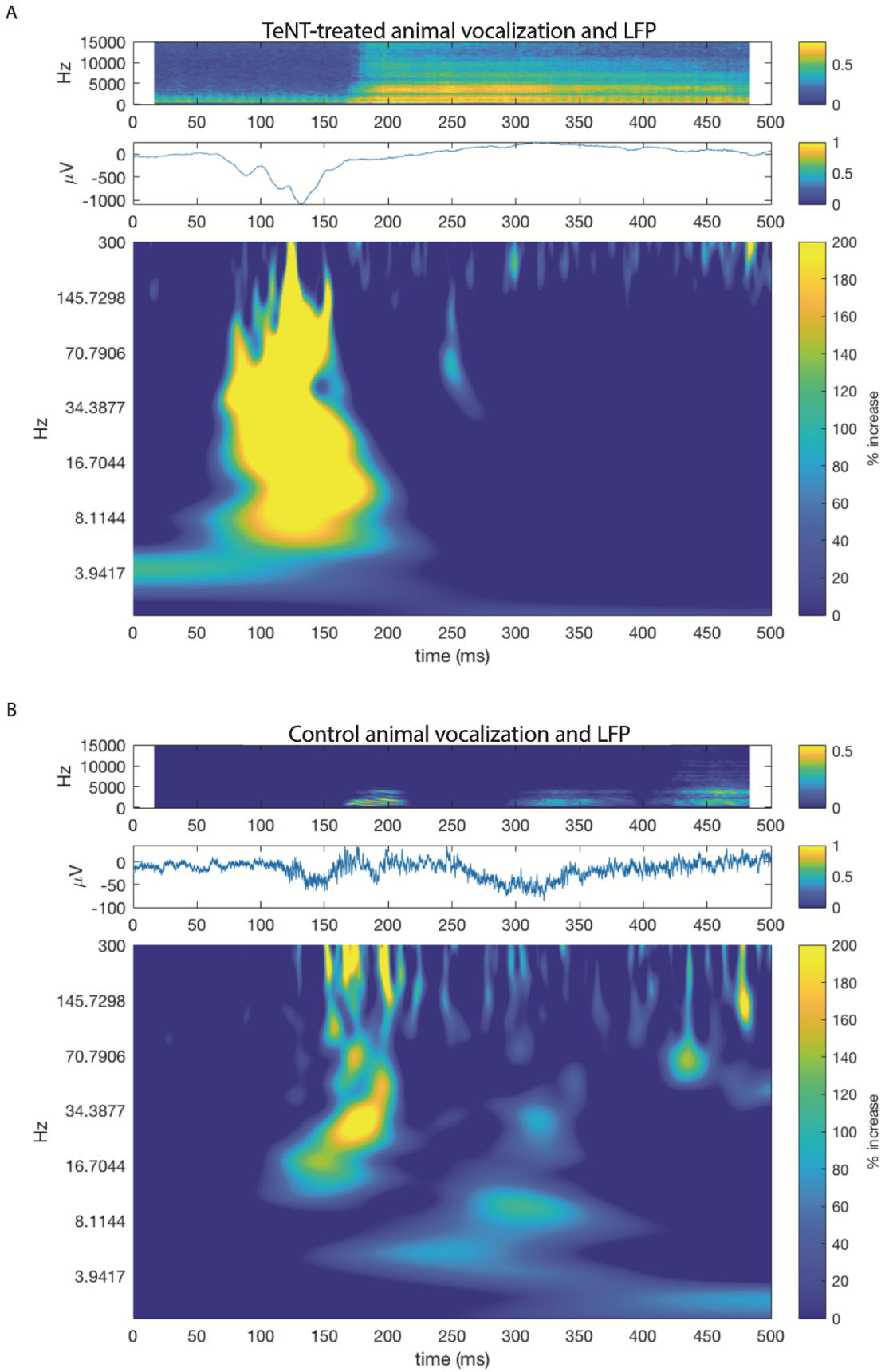

Figure legend on next page.

Supplementary Figure 7: *<u>Example electrophysiology traces averaged over 5 instances of normal or 5 instances of degraded vocalizations.</u>* ***A*** *Averaged spectrogram of degraded vocalization (n=5) 5 days post-electrode-implantation in a chronically recorded TeNT-treated animal. The plot below the spectrogram shows the raw averaged trace of extracellular recording. Below the raw trace is the averaged continuous wavelet transform of the local field potentials (LFP, 1-300Hz). The plots show a large deflection event (similar to those seen during lights-off in Figures 2 and 3) right before the onset of the vocalization in the TeNT-treated animal.* ***B*** *Averaged song spectrogram (n=5) 5 days post-electrode-implantation from a chronically recorded control animal. The plot below the spectrogram shows the raw averaged trace of extracellular recordings. Below the raw trace is the averaged continuous wavelet transform of the local field potentials (LFP, 1-300 Hz). The averaged control song shows more and smaller amplitude deflections mostly during the vocalization compared to the TeNT-treated vocalization.*

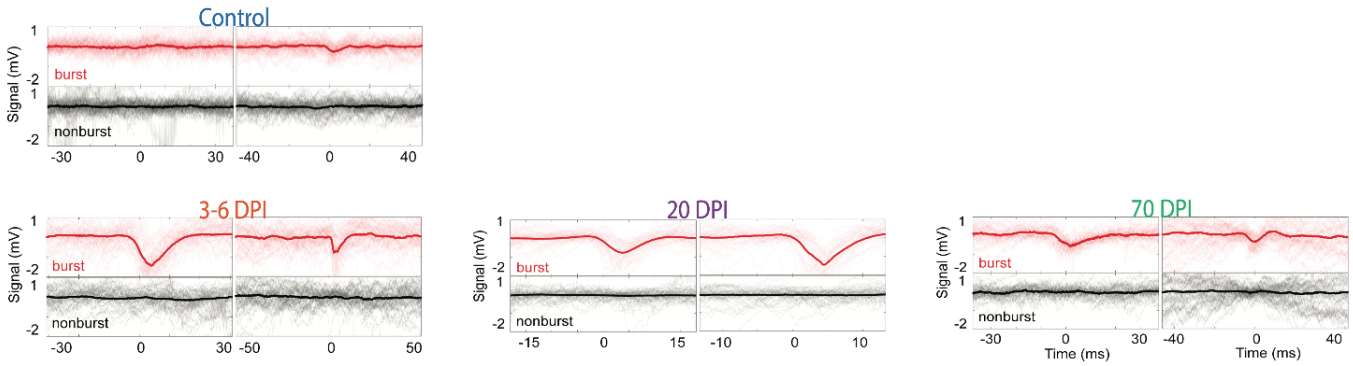

Supplementary Figure 8: *<u>Example traces of raw deflections in the acute Neuropixel recordings during lights-off periods.</u> Control animals barely showed any visible deflection events, while TeNT-treated animals (example traces shown at 3-6, 20, and 70 dpi) displayed large amplitude voltage deflection events.*

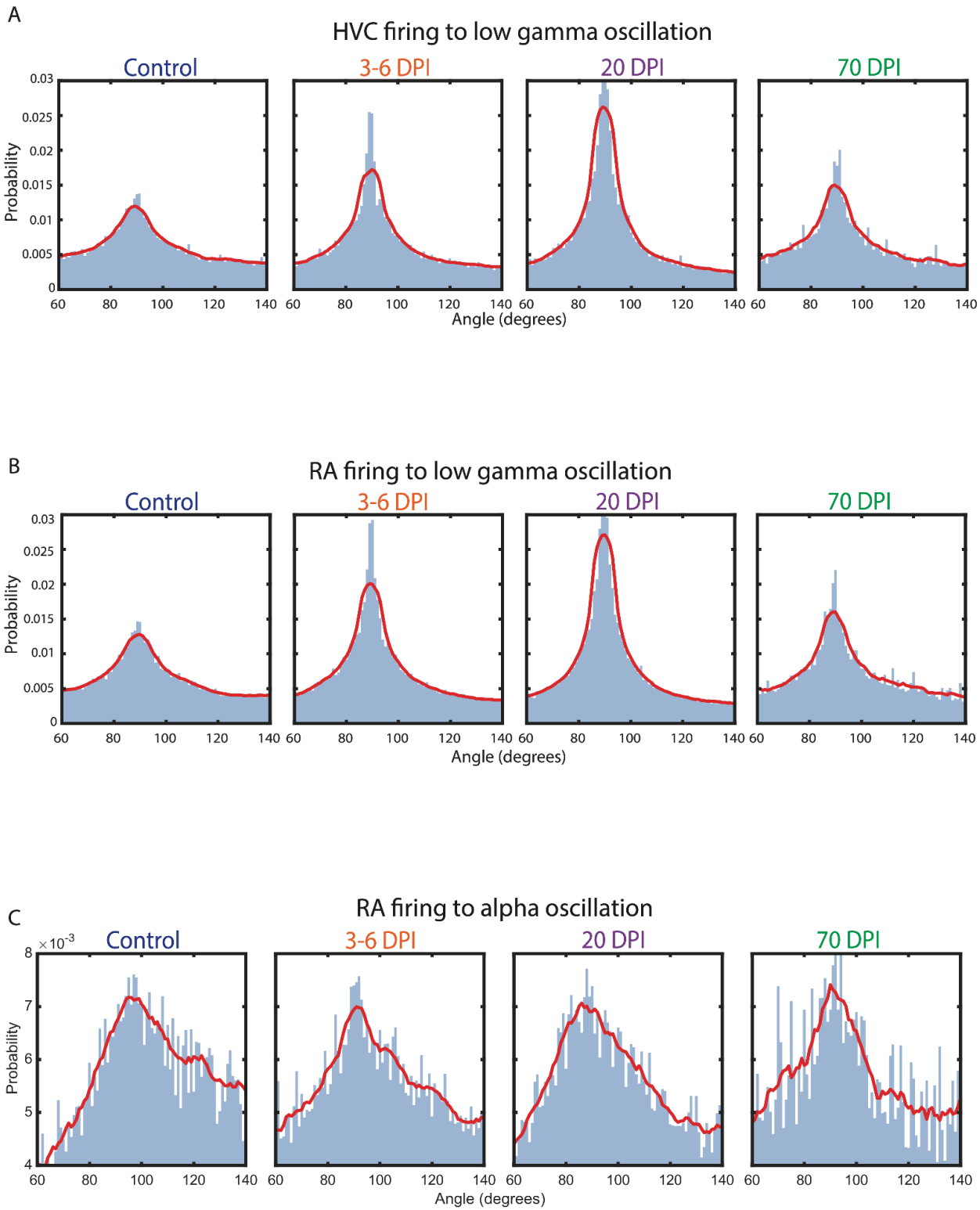

Figure legend on next page.

Supplementary Figure 9: *Relationship between alpha or gamma oscillations during lights-off voltage deflection events and local neuronal firing in HVC and RA from the acute NPIX recordings* ***A*** *The normalized probability distribution of neurons locally within HVC fire during a specific phase (angle) of the gamma (30-40 Hz) oscillations extracted from the LFP signal of the averaged deflection events at 3-6 dpi (n=4 animals), 20 dpi (n=4 animals), 70 dpi (n =2 animals that recovered their song by then). There was a slight change in local neuronal firing to the angle and locking precision to gamma oscillations that resembled control by 70 dpi.* ***B*** *Normalized probability distribution of neurons locally within RA fire during a specific phase (angle) of the alpha (1-10 Hz) oscillations in HVC extracted from the LFP signal of the averaged deflection events at 3-6 dpi, 20, 70 dpi. No change in RA spontaneous neuronal firing to alpha oscillations in HVC during the deflection events over the course of the manipulation.* ***C*** *Normalized probability distribution of neurons locally within RA fire during a specific phase (angle) of the gamma (30-40 Hz) oscillations in HVC extracted from the LFP signal of the averaged deflection events at 3-6, 20, and 70 dpi. We observed no change in RA spontaneous neuronal firing to the gamma oscillations in HVC during the deflection events over the course of the manipulation.*

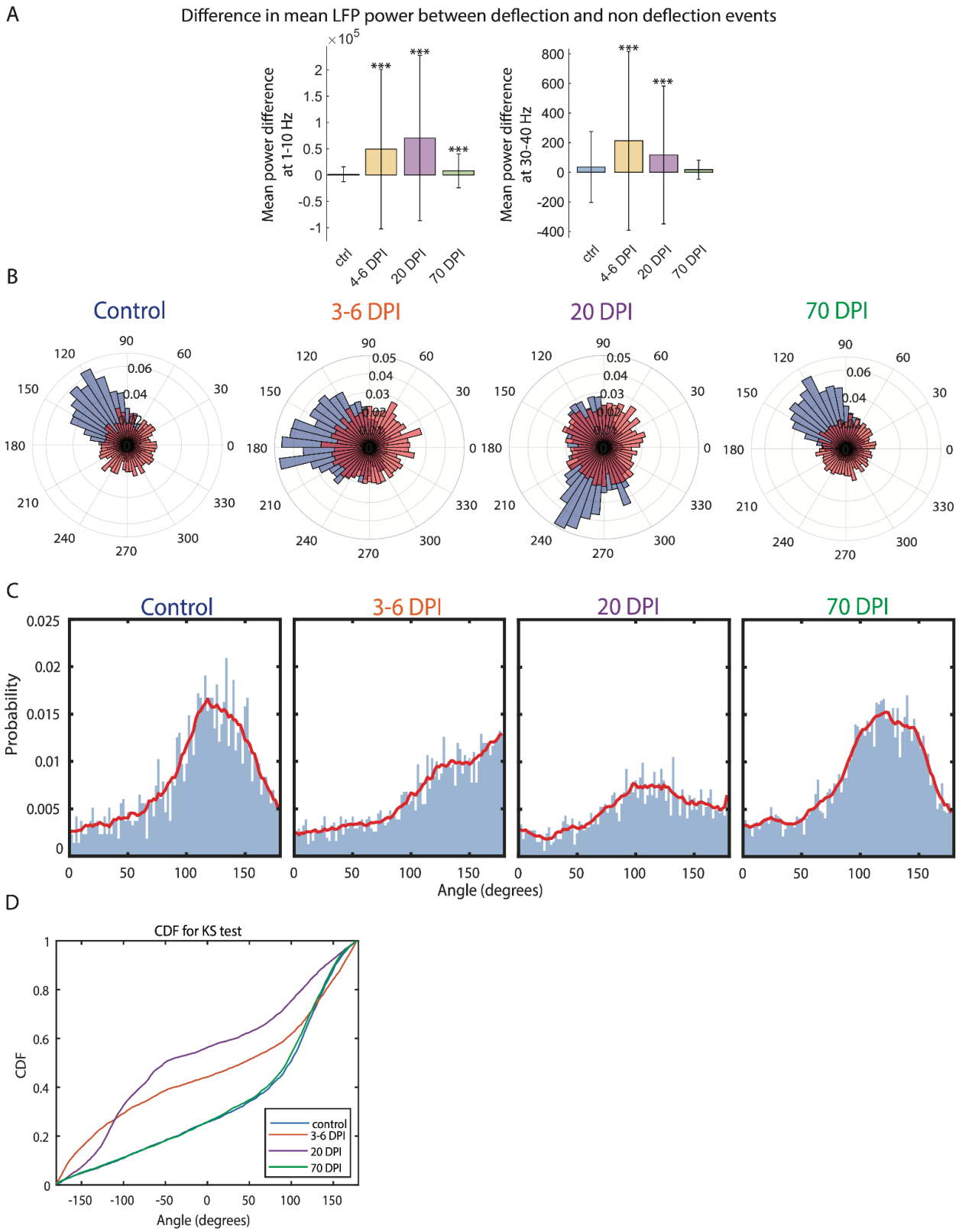

Figure legend on next page.

Supplementary Figure 10: *Quantification of the angle relationship between alpha (1-10 Hz) and gamma (30-40 Hz) frequencies during deflection events in control and TeNT-treated animals during acute head-fixed recordings.* ***A****: The average difference in power (at alpha, 1-10 Hz, and low gamma 30-40 Hz frequency ranges) between voltage deflection and non-deflection events in control, 3-6, 20, 70 dpi. The power content in the alpha range increased in a statistically significant way (Wilcoxon, rank sum test) between control and 3-6 (p=2.9*10^-36), 20 (p=8.6*10^-167), 70 (p=5.4*10^-4) dpi animals. However, the increase in power between control and 3-6 (p=2.2*10^-37), 20 (p=6.3*10^-27) dpi is statistically significant but returns to control level by 70 (p=0.37) dpi. The stars above the bar plots (*) indicate statistical significance (* : p < 0.005, ** : p< 0.01, *** : p < 0.001).* ***B****: The polar histograms of the angle of the low gamma oscillations (1-10Hz) at the maximum amplitude of the gamma oscillation (30-40 Hz) during deflection events. The red distribution represents a randomly shuffled dataset, while the blue is the true distribution of angles in control (n=3), and TeNT-treated animals at 3-6 dpi (n=4), 20 dpi (n=4) and 70 dpi (n=4) during deflection events.* ***C****: Relationship of alpha and low gamma oscillations during deflection events in control (n=3), 3-6 (n=4), 20 (n=4), and 70 (n=2 animals) dpi animals (over animals and conditions). The probability distribution of a specific angle of the low-frequency oscillation at the maximum amplitude of the gamma oscillation.* ***D****: The results of the Kolgomorov-Smirnov test on the cumulative density function (CDF) to assess if the change in probability distribution shown in C is statistically significant from control distributions at 3-6, 20, and 70 dpi. The purple (20 dpi) and orange (3-7 dpi) distributions differ significantly from the blue control and the 70 dpi green distributions. The 70 dpi population is not significantly different from the control group.*

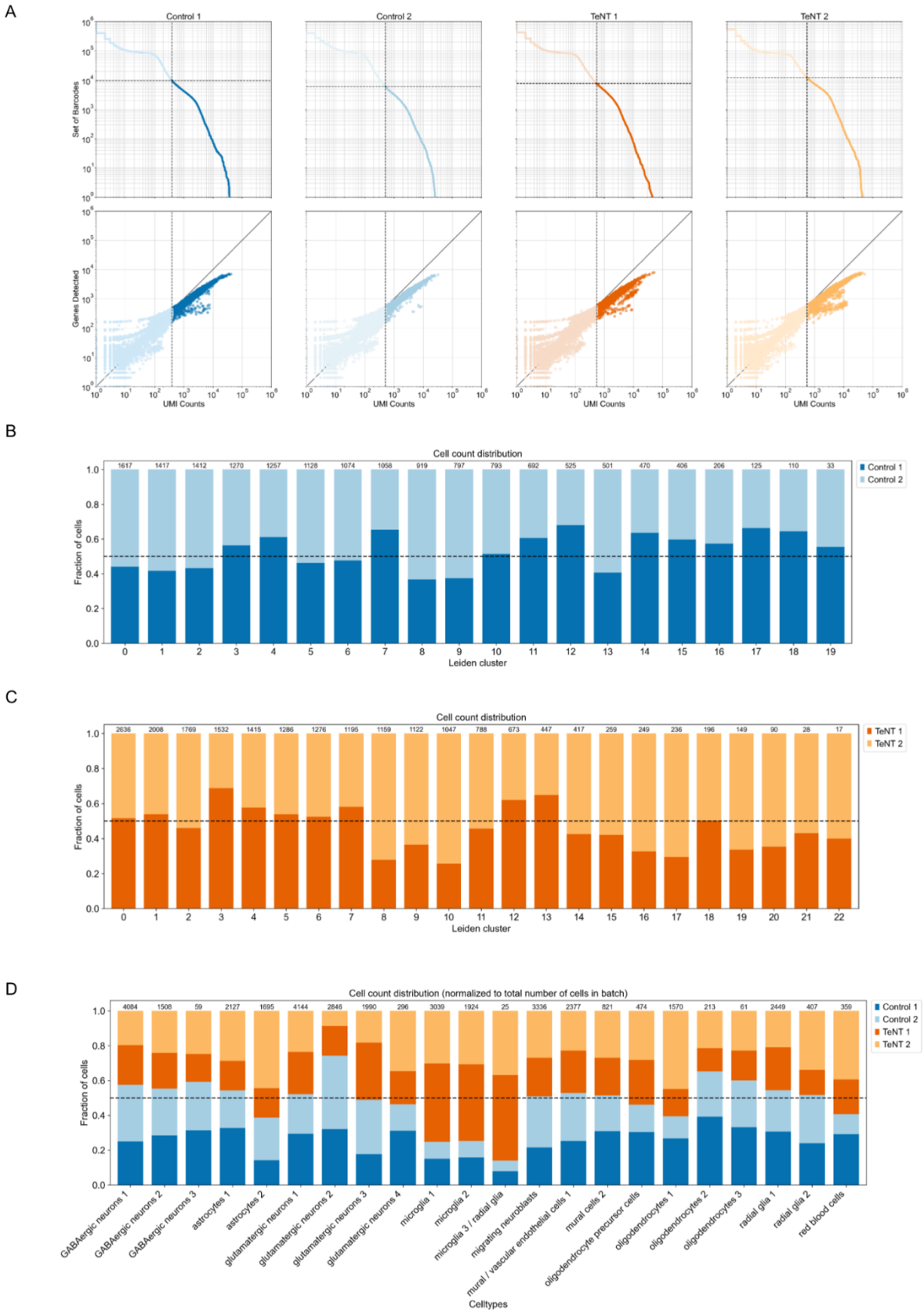

Figure legend on next page.

Supplementary Figure 11: *Quality control of the single-cell RNA sequencing HVC datasets from control and TeTN-treated animals at 25 days post-injection (dpi).* ***A*** *"Knee plots" showing the set of barcodes (top row) and number of genes detected (bottom row) over UMI counts. The dashed lines depict the quality filtering cutoff.* ***B-C*** *Barplot depicting the fraction of cells from each replicate per cluster for control (B) and TeNT (C), normalized (by dividing) to the total number of cells in each replicate. Control and TeNT datasets were clustered separately using the Leiden algorithm. The equal distribution of replicates across the clusters suggests that technical effects do not dominate the clusters. Thus, we did not perform batch correction. The numbers on top of the bars indicate the total number of cells in each cluster.* ***D*** *Barplot depicting the fraction of cells from each dataset in the cell type clusters obtained after jointly clustering the control and TeNT datasets. The numbers on top of the bars indicate the total number of cells in each cluster.*

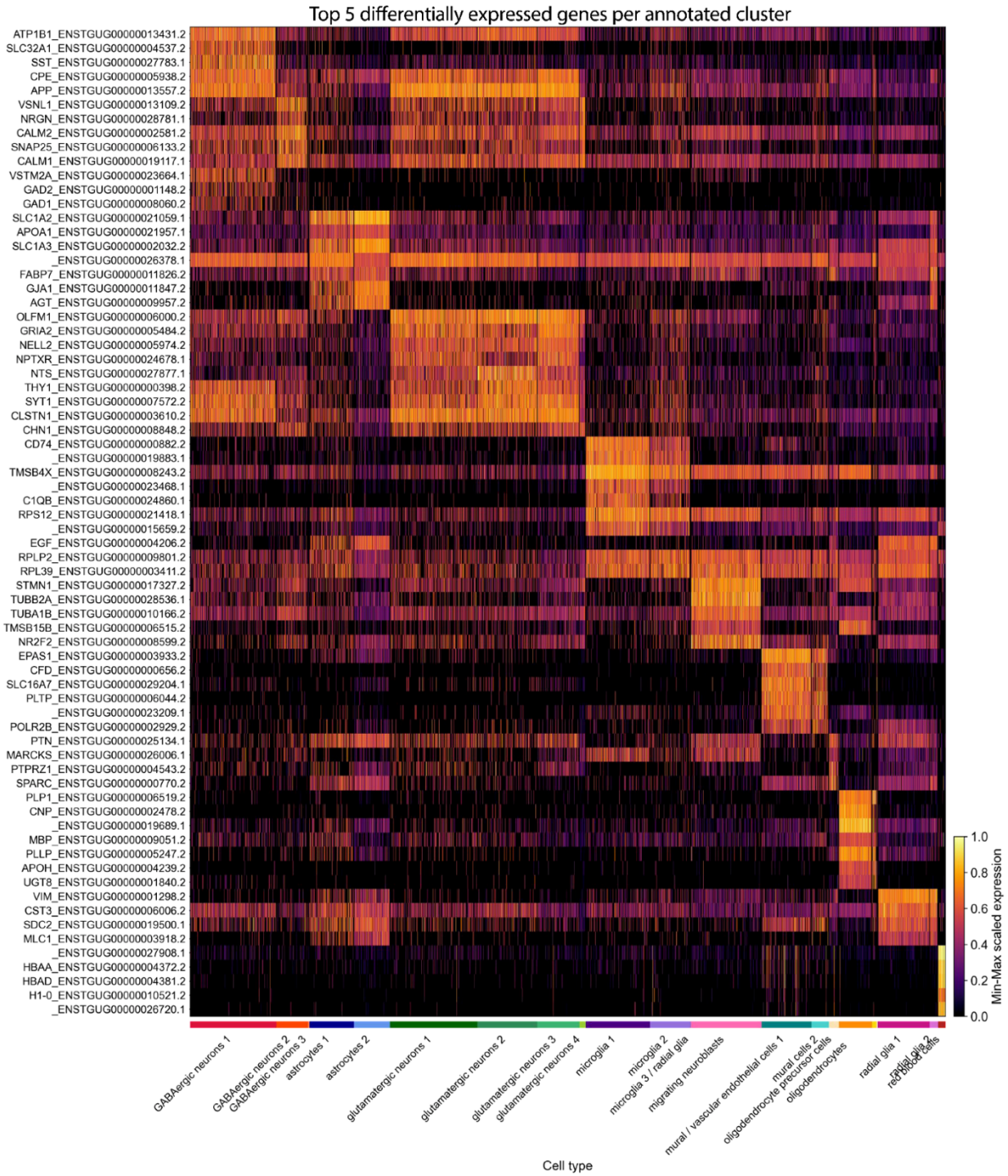

Supplementary Figure 12: *<u>Heatmap of top 5 differentially expressed genes per annotated cell type/cluster obtained by single-cell RNA sequencing of HVC from control and TeNT-treated birds at 25 dpi.</u> Differentially expressed genes between clusters were identified using Scanpy's rank_genes_groups (p values were computed using a t-test and were adjusted with the Bonferroni method for multiple testing. They were then confirmed by comparison to p values generated with the nonparametric Wilcoxon test with Bonferroni correction). The heatmap depicts the min-max scaled expression for each gene.*

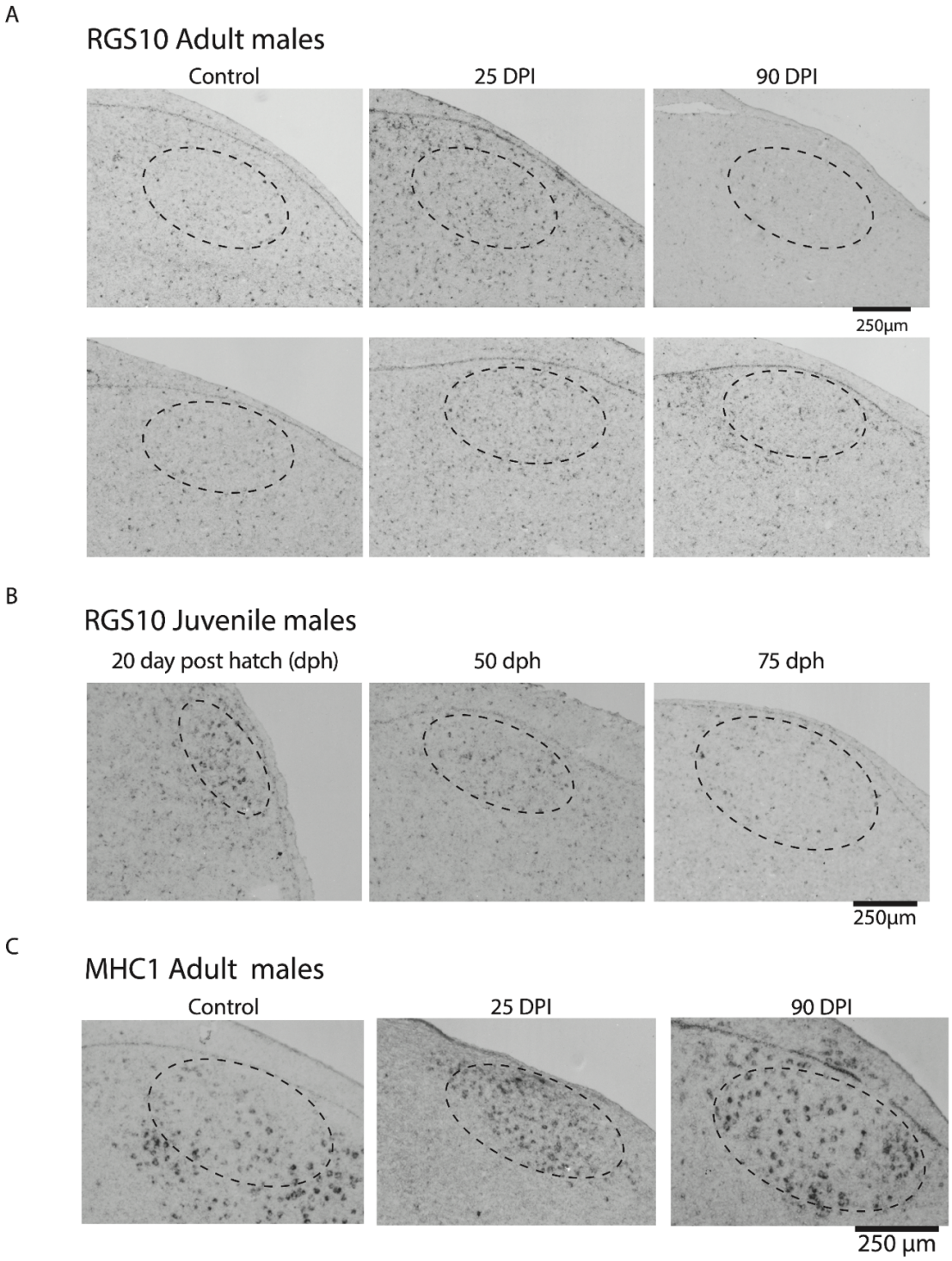

Supplementary Figure 13: *<u>In situ hybridization of microglia marker gene RGS10 in adult male control, TeNT-treated and juvenile male HVC & MHC1 gene in adult male control and TeNT-treated HVC.</u>* ***A*** *Histological sections of HVC (in control and TeNT-treated animals at 25 and 90 dpi) after in situ hybridization of RNA probes for RGS10 (a gene marker for microglia).* ***B*** *Histological sections of HVC in naive juvenile males (at 20, 50, and 75 days post-hatching (dph)) after in situ hybridization of RNA probes for RGS10.* ***C*** *Histological sections of HVC (from control and TeNT-treated animals at 25 and 90 dpi) after in situ hybridization of RNA probes for MHC1. Black/darker dots indicate enzyme reactions resulting in successful probe localization and suggest target gene expression.*

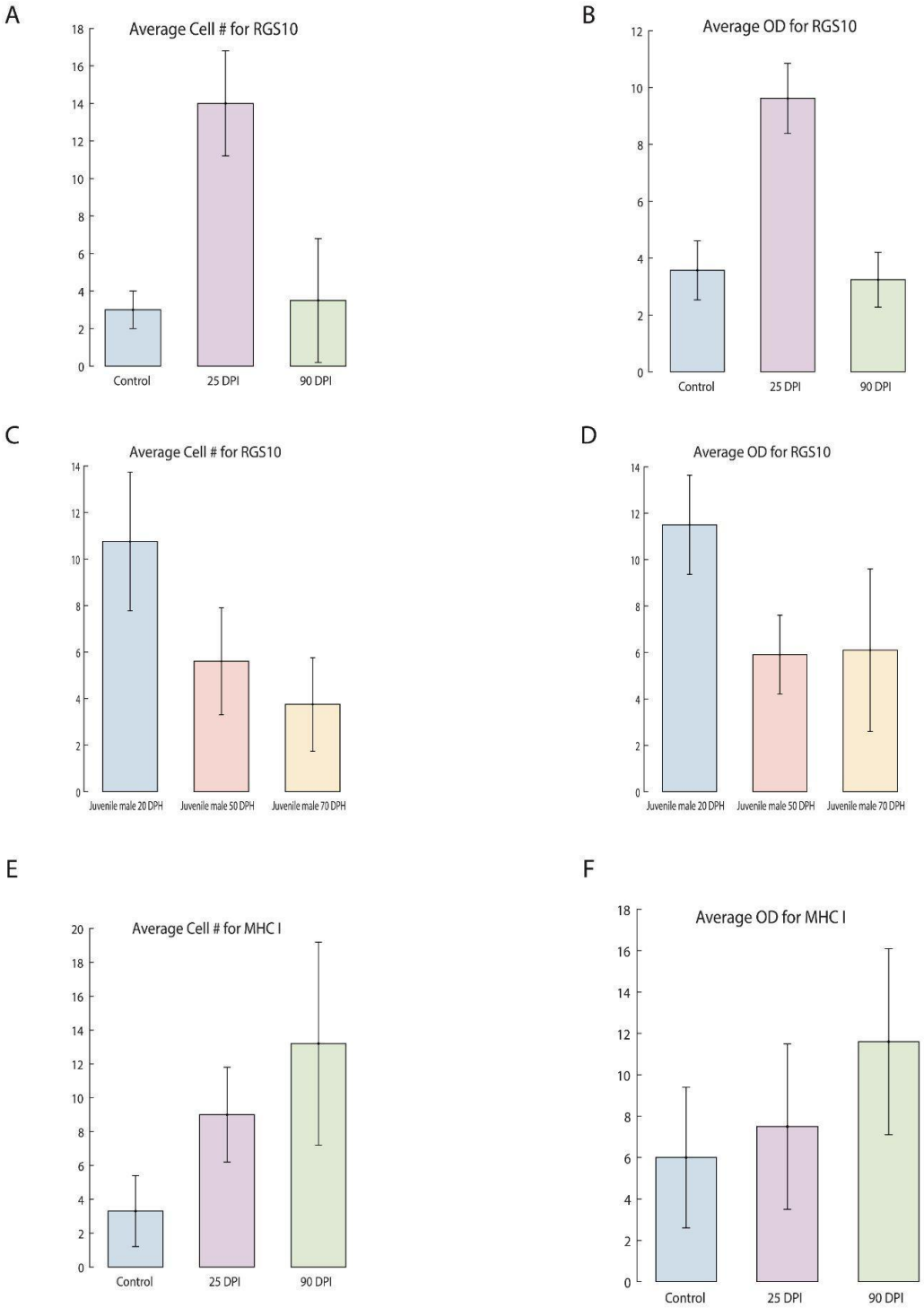

Supplementary Figure 14: *Quantification of the in situ hybridization against microglia marker gene RGS10 in adult male control, TeNT-treated and juvenile male HVC; and MHC1 in adult male control, TeNT-treated animals.* ***A-B*** *Quantification of the in situ hybridization for RGS10 between control (n=4 animals) and TeNT-treated animals at 25 dpi (n=4) and 90 dpi (n=4).* ***C-D*** *Quantification of the in situ hybridization for RGS10 between juvenile males at 20, 50, and 70 days post-hatching (dph) (n=4).* ***E-F*** *Quantification of the in situ hybridization for MHC1 between control (n=4) and TeNT-treated animals at 25 (n=4) and 90 dpi (n=4). Error bars represent standard deviation.*

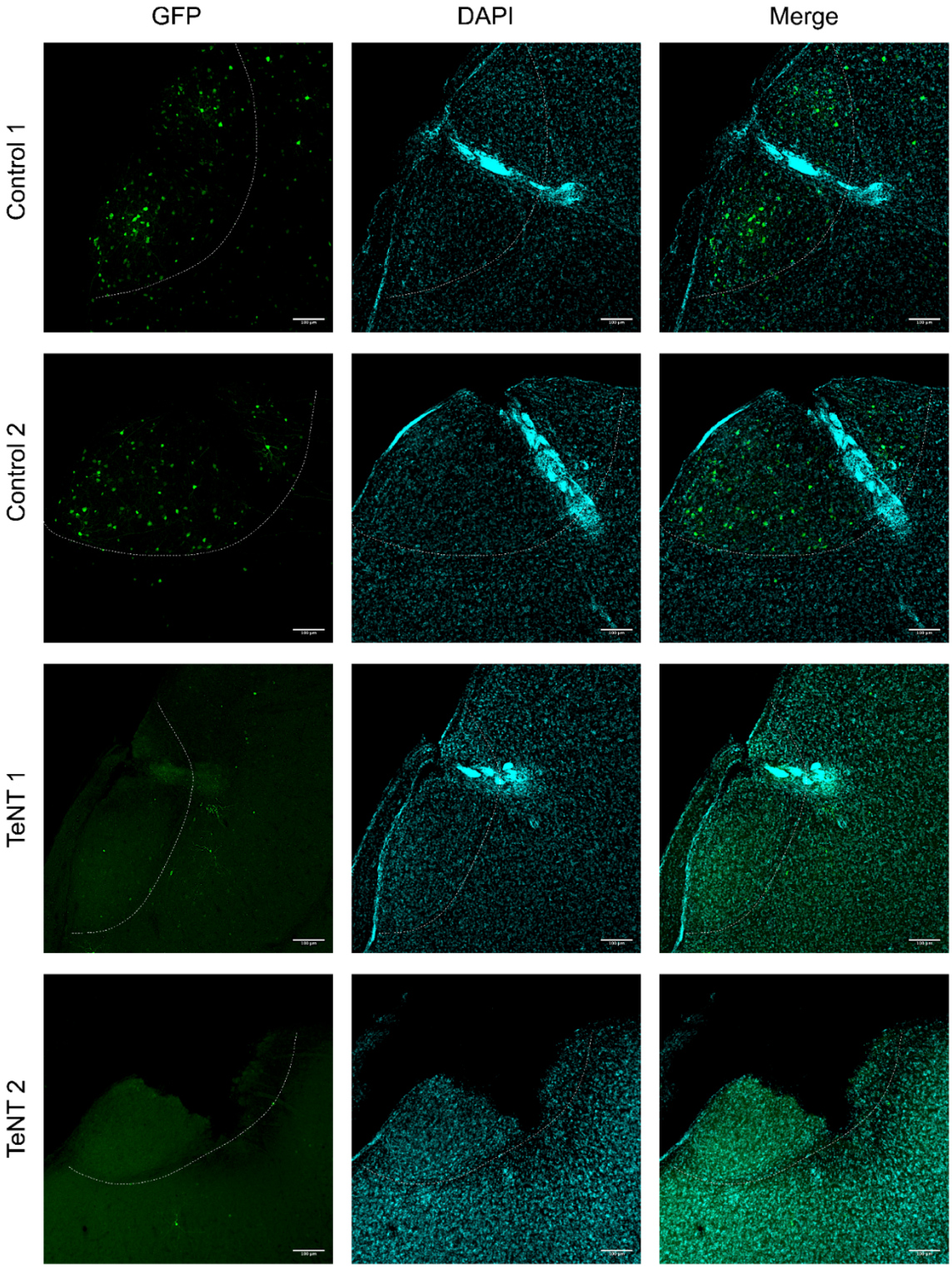

Supplementary Figure 15: *Histology of electrode array location in HVC in the chronically implanted animals. The white dotted line outlines HVC. Some sections display missing tissue due to the removal of the electrodes after perfusion of the animals. The stronger cyan signal indicates glial scar formation around the electrode array, which provides an approximation of the location of the electrodes.*

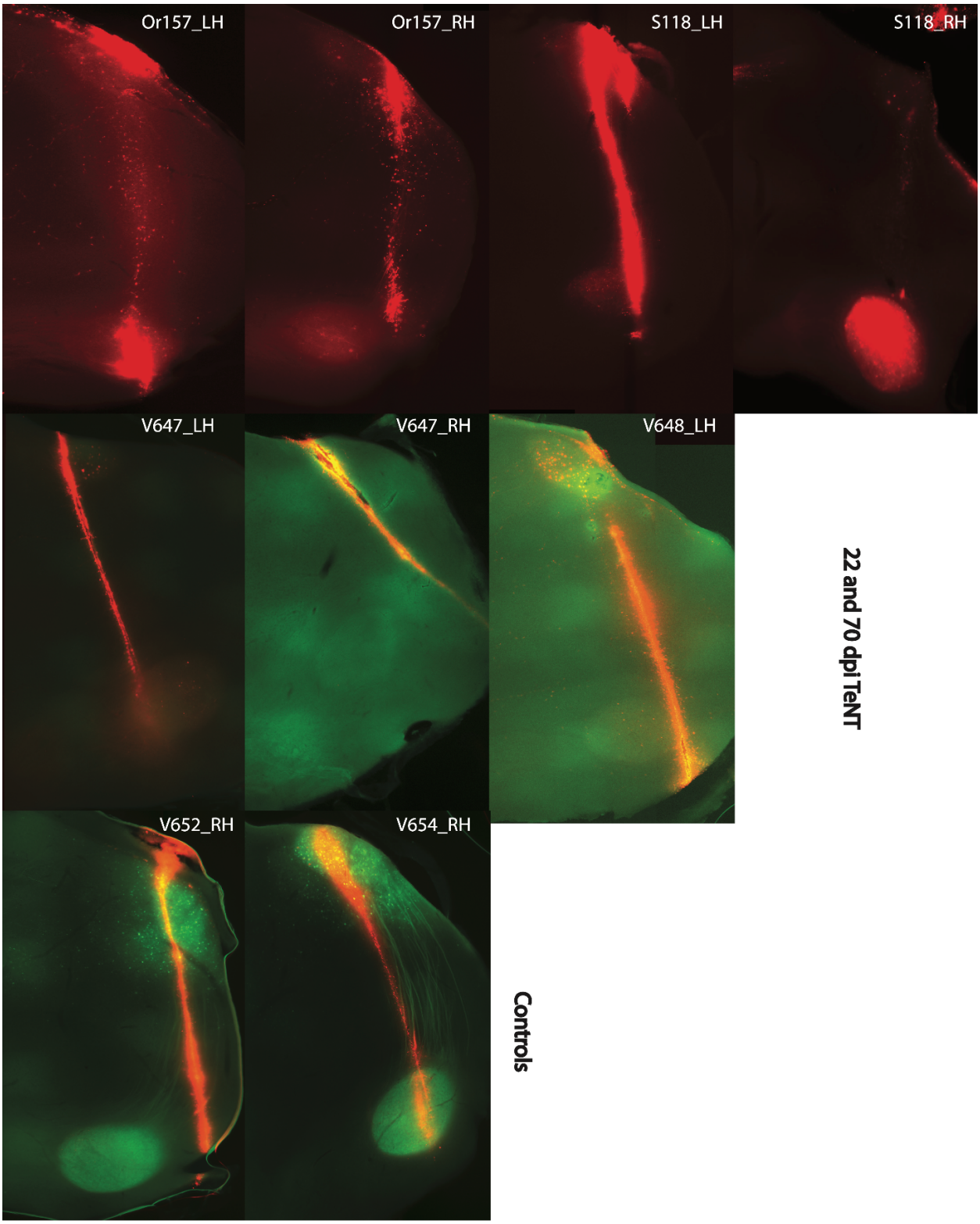

Supplementary Figure 16: *Histology to confirm the high-density silicone electrode location in the acute head-fixed animal recordings. The red trace represents the electrode location. The green trace represents the second*

electrode location in animals that were recorded twice, 40 days apart. The white labels represent the animal IDs. "LH" and "RH" stands for left and right hemisphere, respectively.

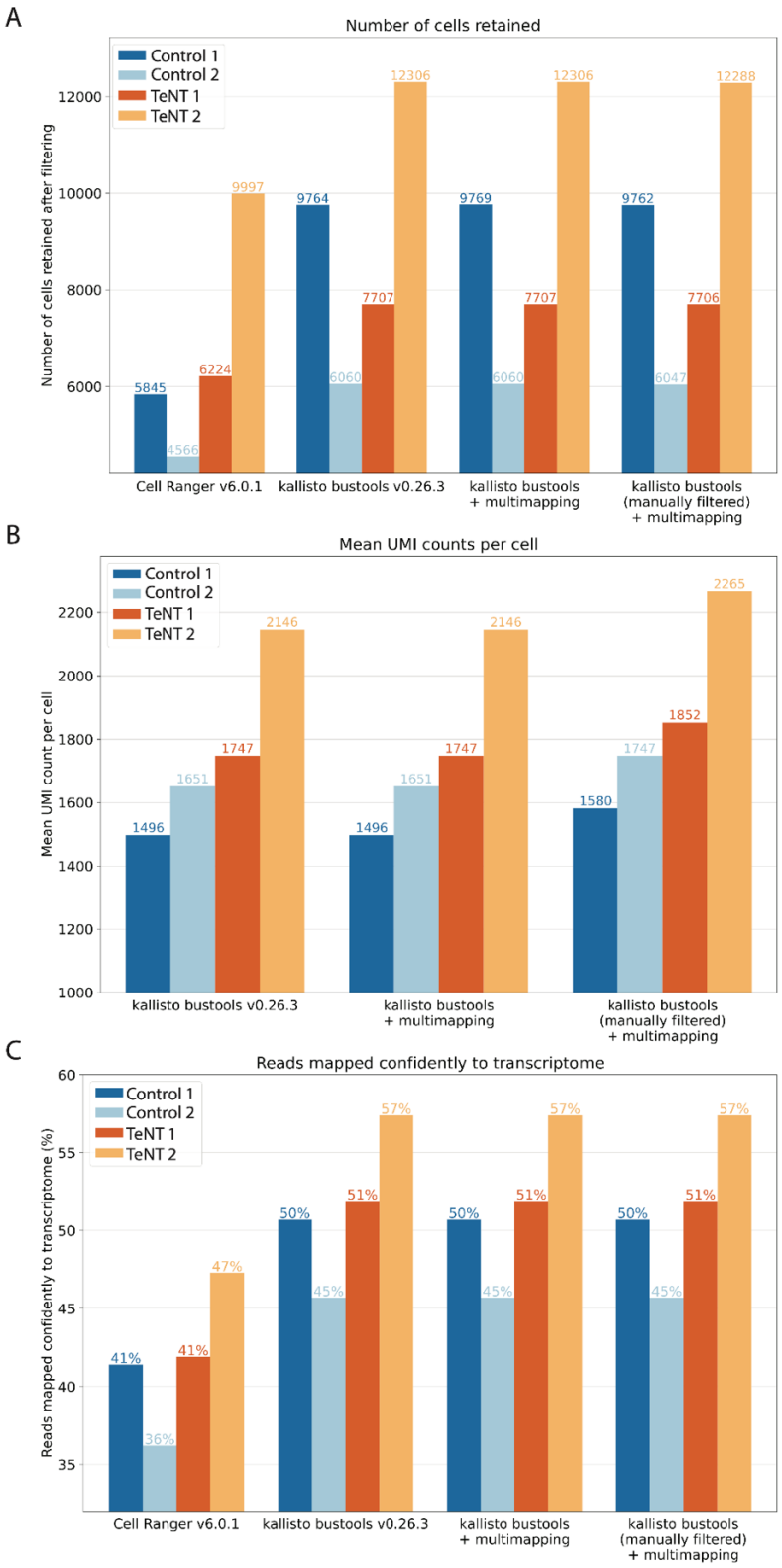

Figure legend on next page.

Supplementary Figure 17: *Comparison of different pre-processing methods for the HVC single-cell RNA sequencing datasets.* ***A*** *Number of cells retained after quality control for each dataset and alignment method.* ***B*** *Mean UMI counts per cell for each dataset and pre-processing method.* ***C*** *Percentage of reads confidently mapped to transcriptome for each pre-processing method.*

A

Deflection durations (half-widths) in ms (mean ± SD)						
	3-5 DPI	15 DPI	30 DPI	45 DPI	60 DPI	75 DPI
Control animal 1 (OR295)	44.2083 ±16.0885	50.7321 ±21.5322	47.7079 ±16.4028	49.5889 ±18.5678	45.4170 ±15.4166	48.2883 ±18.5856
Control animal 2 (PK31)	43.9120 ±15.5607	46.5072 ±17.6237	36.7974 ±15.6453	42.4989 ±15.8985	37.8048 ±15.2497	35.3157 ±15.2297
TeNT-treated animal 1 (B138)	24.7074 ±11.0296	20.4568 ±5.7482	26.2938 ±10.4427	32.1460 ±13.1017	36.8212 ±15.3777	41.4122 ±15.9937
TeNT-treated animal 2 (OR296)	34.6744 ±10.7396	29.2852 ±8.3464	29.5713 ±9.5446	31.4171 ±11.5461	39.8151 ±10.5067	42.9507 ±14.0682

B

Deflection amplitudes in µV (mean ± SD)						
	3-5 DPI	15 DPI	30 DPI	45 DPI	60 DPI	75 DPI
Control animal 1 (OR295)	-136.3911 ±28.7491	-155.0317 ±49.3434	-151.5708 ±35.8116	-149.0358 ±34.9365	-152.4109 ±33.1907	-150.5303 ±33.8846
Control animal 2 (PK31)	-111.9867 ±20.8258	-117.1694 ±26.5227	-133.9981 ±26.5174	-130.6166 ±25.9310	-138.6591 ±26.7510	-135.2756 ±25.9969
TeNT-treated animal 1 (B138)	-538.6617 ±307.8410	-816.7580 ±371.9481	-705.8811 ±267.1738	-422.1097 ±143.1100	-306.8821 ±101.9335	-261.2531 ±80.5379
TeNT-treated animal 2 (OR296)	-174.6613 ±39.6156	-251.7470 ±70.1546	-337.3158 ±94.5369	-525.5973 ±157.8933	-228.3434 ±48.9163	-162.6949 ±35.6879

Table legend on next page.

Supplementary Table 1: *Amplitudes and durations of the chronic voltage deflections measured throughout the recording.* ***A*** *Mean duration (calculated as the distance from the onset to the half-width point of the event) in ms of voltage deflection events with standard deviation, each row represents an event from one control (Or 295, PK31) or TeNT-treated (B138, Or296) animal. The data was sampled at 3-5, 15, 30, 45, 60, and 75 dpi.* ***B*** *Mean amplitudes (in µV) of voltage deflection events with standard deviation.*

Dataset (short name)	Species	Condition	Brain area	Replicate #	Technology	Pre-processing tool	# of cells retained after QC	Sequencing depth (number of reads processed)	Reads mapped confidently to transcriptome (%)	Mean UMI count per cell	Total UMI count
C1	Taeniopygia guttata	cag-neonGreen	HVC (both hemispheres)	1	10xv3	kallisto bustools	9,763	744,473,151	50.7	1580.8531	15,433,015
C2	Taeniopygia guttata	cag-neonGreen	HVC (both hemispheres)	2	10xv3	kallisto bustools	6,047	787,232,472	45.7	1747.639	10,568,132
E1	Taeniopygia guttata	dlx-TeNT-GFP	HVC (both hemispheres)	1	10xv3	kallisto bustools	7,706	867,768,600	51.9	1852.4215	14,274,784
E2	Taeniopygia guttata	dlx-TeNT-GFP	HVC (both hemispheres)	2	10xv3	kallisto bustools	12,288	810,253,355	57.4	2265.4258	27,837,586

Supplementary Table 2: *Overview of single-cell RNA sequencing datasets.*